Photovoltaic Applications in Light Communication Systems

Ioannis Skourtis, *MSc Thesis in Electrical Power Engineering*

PVMD Group, TU Delft

Student Number: 5134749

PVMD Group

Photovoltaic Applications in Light Communication Systems

by

Ioannis Skourtis

A thesis submitted in partial fulfilment

of the requirements for the degree of

Master of Science

in

Electrical Engineering

at the Delft University of Technology,

to be defended publicly on April 22nd, 2022

Student Number: 5134749

Thesis committee:

Prof. Dr. Olindo Isabella,	TU Delft, Professor
Dr. Marco Zuñiga	TU Delft, Associate Professor
Dr. Patrizio Manganiello	TU Delft, Assistant Professor
Dr. Mirco Muttillo,	TU Delft, Postdoctoral researcher

This thesis is confidential and cannot be made public until April 22nd, 2024.

Table of contents

Photovoltaic Applications in Light Communication Systems

Abstract---This thesis project explores the role of photovoltaics in visible light communication (VLC). It focuses on the development of a theoretical model suitable for the study of various photovoltaic (PV) technologies in their role as a receiver in light communication systems. These photovoltaic technologies are characterized based on the energy which they are able to harvest as well as their bandwidth, to quantify the achievable transfer rate for the different photovoltaic technologies. The AC equivalent circuit is considered, where the solar cell capacitance depends on its operating point. A fitting is made of the model with the experimental results in order to estimate the dynamic parameters of different solar cells that were already available in the laboratory of the Photovoltaic Materials and Devices (PVMD) group. To characterize the dynamic behavior of solar cells, an ad-hoc test bench will be realized.

1. INTRODUCTION

1.1 Visible Light Communication

Humanity's ever increasing demand for network capacity has caused the emergence of a number of technologies capable of meeting it. Wireless communications have become essential in the past 30 years, with radio-frequency (RF) technologies driving progress in the field. However, the limited capacity of RF technologies creates a natural boundary in the maximum supply of electromagnetic spectrum. Hence, optical wireless communications (OWC) has been developed in order to allow for data transmission using optical carriers in the visible, infrared (IR) and Ultraviolet (UV) spectrum.

Light Fidelity (Li-Fi) is an OWC technology that uses light-emitting diodes (LEDs) for data transmission and photodiodes (PDs) for data reception in indoor environments [1]. This is the conventional setup employed by Li-Fi technologies and employs either positive-intrinsic-negatives (PIN) or avalanche photodiodes which offer high bandwidth.

For outdoor communication applications this setup is problematic, since it requires an external power source for the operation of the photodiodes. Additionally, the variability of the irradiance of natural sunlight may be problematic, possibly saturating the receiver. In order to solve the aforementioned issue, alternatives have been tried, i.e. lasers for data transmission and photovoltaic cells for receiving data [1].

The main advantage for using PV cells for outdoor Li-Fi communications is the fact that they do not require an external power source [2], as they are simultaneously used for energy harvesting and data reception. The ability of photovoltaics to convert an optical signal to an electrical signal, while harvesting energy, is a major advantage this thesis project relies upon. Additionally, PV panels have a minimal requirement for beam tracking, namely to ensure that light transmitted from the light source indeed is aligned and reaches the receiving cell, as opposed to photodiodes, where this is a concern. Evidently, the reason is the size of PV panels versus PDs. PVs also do not require a transimpedance amplifier circuit, which is the case with photodiodes due to their small output current. That circuit it usually more expensive than the electronics circuit needed for information reception using photovoltaics. On the contrary, the larger area of PV cells has the potential drawback of signal jamming, namely higher likelihood of signal interference, and also makes eavesdropping easier. Bandwidth is also lower than in the case of photodiodes [3].

The type of photovoltaic cells which can be used for visible light communication is not restricted to the conventional Si solar cells. Thin film cells as well as perovskite solar cells have also been used [4]. Thus, not restricting one's research to one type of cell is beneficial. Wang et al [5] were few of the earliest to successfully establish communication using a white LED for data transmission and a poly-Si panel for receiving

data. Alternative PV cells are typically smaller in size which yields lower capacitance but makes the alignment requirements for communication stricter. Hence, a tradeoff between PV cell size and alignment requirements exists. Since PV cell size have a positive correlation with energy harvested, the tradeoff therefore exists between alignment and energy harvested.

1.2 VLC communication data rates

In terms of data rate of communication, in most cases solar cells provide a sufficient data rate of the order of magnitude of a few Mbps. The link distance, i.e. the distance between the transmitter and the receiver, used by Wang et al [6] is 1m and even Fakidis et al [7] who set the record for the data rate of 522 Mbps, achieved it at 2m link distance. In reality, longer link distances may be required. As a result, the first ever prototype was invented in 2019 by Das et al [8] establishing outdoor communication at a link distance of 30m. It was tested at the University of Edinburgh and installed in Scotland on the Orkney Islands.

This type of of free-space optical (FSO) wireless communication had never been successfully established with lasers and solar cells. The purpose of the system was to provide Internet access to two homes on the island. The maximum achieveable data rate came out to be 8Mbps. Carefully selecting the transmitter wavelength is important as demonstrated by Das et al [8]. In cases where conventional LED data transmitters are used, 1550nm wavelength seems to be optimal due to the high maximum permissible exposure of 100mW/cm^2. However, when using Si solar cells, as in the aforementioned study which took place in Scotland, somewhere in the range of 900-1000nm peak responsivity is obtained.

Moreover, it is advisable that the transmitter is capable of sending a divergent laser beam that covers the whole PV panel. Possible misalignment may be caused due to weather conditions (which are a consideration, as PV panels are advantageous for use in VLC outdoors) and the laser beam being divergent is a way to account for it. Another requirement of the system is the ability of the transmitter to dynamically control the power of the signal based on weather conditions [8].

Delving more into the operation of the PV panel for data reception, it is worth noting that solar cells have a low-pass frequency response. The frequency response of a typical silicon solar cell is shown in figure 1:

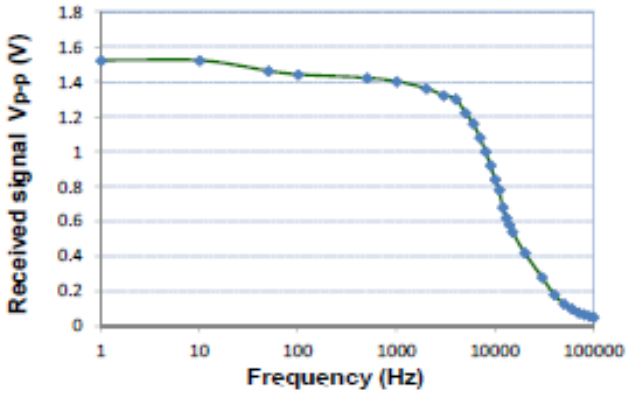

Figure 1. Example of a frequency response of a 27 X 27 mm silicon solar cell [9]

In figure 2, which is a generic VLC system architecture, the signal is represented as a current source. Once the signal, both DC and AC, has been received by the solar cell, it is separated through an AC/DC decoupling circuit. Then, we extract the information from the AC signal. The overall system architecture in general when utilizing solar cells in VLC for both energy harvesting and communication receiver is shown in figure 2:

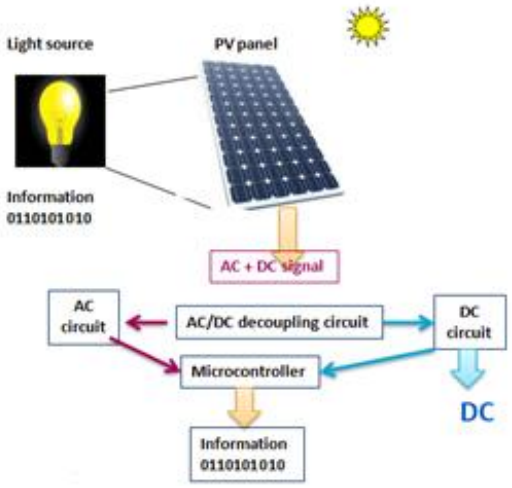

Figure 2. Generic VLC System Architecture

Dal et al's setup was rather complex, since they included FPGAs and DAC as well as ADC. The FPGAs receive the information packet of the signal and convert it to a time-based signal using OFDM modulation technique. The DAC is then used to convert from digital to analogue waveform, whereas in the opposite direction the ADC is utilized to perform the analogue back to digital conversion. Another similarity between most research test benches and ours is the use of an AC-DC separating circuit first used by Wang et al [6].

Link distance seems to be a confounding factor, when examining the results the majority of research groups obtained. Specifically, the data rate in Mbps is vastly dependent on the link distance. The longer the link distance, the harder it is to achieve high data rates.

Fakidis et al [7] did achieve a 1 Gbps data rate but the link distance used was merely 40cm which is really not applicable to real world communication requirements. They utilized a solar panel with 36 cells connected in series that is considered 35 times superior in terms of bandwidth compared to a solar cell with 5 or 6 cells connected in series. It offered a 3-dB total bandwidth of 350 kHz. Zhang et al [10] in 2015 showed that organic solar cells are capable of achieving high speed data detection. They developed a 1m wireless laser link and their results were more than satisfactory, achieving a 34Mbps of data rate and a harvested power in the order of mW. A pattern seems to emerge and verify the fact that realistic link distances have only recently started being implemented with the prototype in Scotland described by Dal et al being the leader. Mica et al [4] employed perovskite cells and managed to obtain an excellent data rate of 53 Mbps, however the link distance used was again only 40cm.

Significant progress on the use of photovoltaics on Li-Fi are made by Haas et al [11]. Using a link of the IR-region of the spectrum and a distance of 2m a very high data rate of 522Mbps was accomplished. A GaAs PV cell was used that is single-junction cell designed for maximum efficiency under monochromatic illumination. Through matching the photon energy with the semiconductor bandgap, thermalization losses are kept to a minimum; minimization of transmission losses also plays a role.

A barrier that became evident early in the research of the role of PV cells as data receiver is the tradeoff between harvested energy and information transfer [12]. Fakidis et al [7] employed modification in the peak-to-peak amplitude of the OFDM signal over the I-V curve of the cell. Fakidis achieved great results in optimizing for both with State of the Art Optical Simultaneous Wireless Information and Power Transfer (SWIPT) with 2m link distance end-to-end DC power efficiency of about 10%, 784Mbps data rate and harvested power of 1mW. This is indeed an achievement, but is only marginally better than prior recorded results. It is worth noting that in fact, a maximum data rate of 1041 Mbps was possible, albeit with diminished electrical DC power.

In conclusion, PV panels are capable of powering long-distance communication at low cost and seem optimal for rural communities, where there is scattered demand for connectivity. The reduced cost, as well as the lack of need for accurate alignment between transmitter and receiver makes future research in PV applications in light communication certainly worthwhile. Complex power delivery infrastructure is also not necessary due to the energy harvesting capabilities of solar cells. Of special promise seems the installation of PV systems on rooftops, thus multiplying independent receiver elements' link capacity.

Nonetheless, several issues that have not been tackled in this field of research remain. There is little work that has been done to directly compare different types of solar cells for both energy harvesting and communication purposes. Similarly limited is the research on the effect of varying the operating point of the solar cell as VLC receiver on various modelling parameters.

There are three basic research questions that we address in our research.

- What type of solar cell is preferable for energy harvesting, for communication and for both

- What is the relationship between energy harvesting and communication?
- How do solar cells behave as VLC receivers?
- How does the operating point of the solar cell influence communication?

We followed several steps to answer them. First and foremost, we examine what type of solar cell is best for both energy harvesting and communication. We realize and subsequently delve into the inherent tradeoff between them. Furthermore, we address how parameters of an AC equivalent circuit of a solar cell, such as dynamic resistance and capacitance, including diffusion and junction capacitance, change with bias voltage. We also delve into how bandwidth in AC changes when we change the operating point of the solar cell using a resistive load.

We devise models that describe the behavior of solar cells in communication and energy harvesting. One is the AC model designed to describe solar cells for the purpose of communication. The other model that combines AC and DC is applicable to both energy harvesting and communication. Then we adjust our model including the resistive load to obtain an accurate fitting of the experimental results we collect.

2. VLC MODELLING

Performance models for photovoltaic systems have been developed very early on in solar cell research [13]. Generally, there are three categories for module performance models [14]. First of all, there are the point models, which describe cardinal points on the I-V curve, such as the Sandia model (2004), the Huld model or the single-point efficiency model (SPOC) which is solely used in PV analysis when there is a lack of the data necessary to use other models. Secondly, there are the data-based models, which are based on solar cell or panel data and other data. Finally, there are the equivalent circuit models that describe the full I-V curve at desired irradiance and temperature conditions. The most well-known and widely used model for PV cells in this category is the single-diode model which is derived from the equivalent circuit for a single PV cell. We intend to employ the equivalent circuit model, also known as the five-parameter model, in our research of PV applications in light communication systems, so we hereby expand on it further.

The current-voltage relationship may be based on a model called the single diode model with five-parameters. A basic prerequisite for the five-parameter model is to obtain data from the PV manufacturer. The five-parameter model accurately describes the behavior of I-V, and thus P-V curves, maximum power point (MPP) voltage and current, short-circuit current and open-circuit voltage for various irradiation levels and cell temperatures.

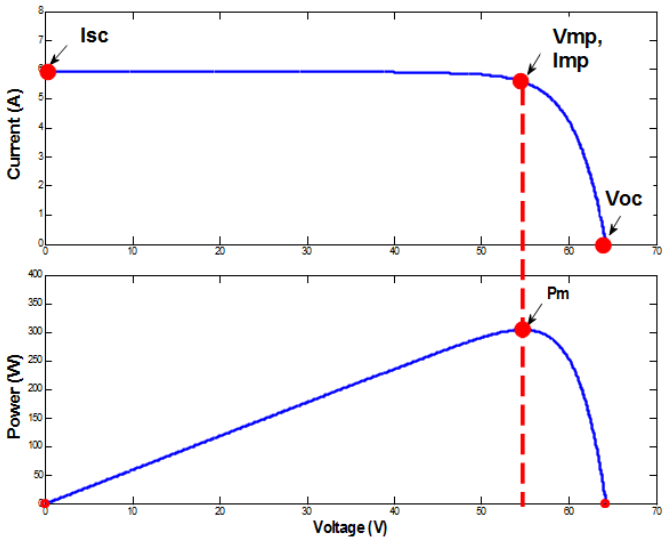

Figure 1: Typical I-V & P-V curves

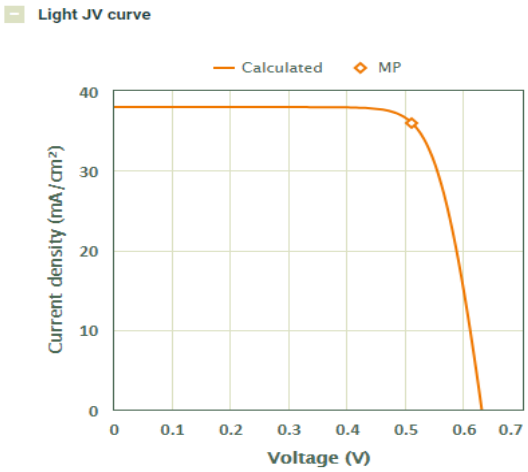

Figure 2: Illuminated J-V curve for the given set of inputs – PV Lighthouse Tool

Overall, the five-parameter model employs the standard parameters, namely short-circuit current (I_{SC}), open-circuit voltage (V_{OC}) and maximum power point conditions (I_{MPP} and V_{MPP}), as well as the series resistance Rs and the shunt resistance Rsh.

2.1 PV Modelling for Energy Harvesting

The aim of our modeling, is to explore possible circuits we could employ depending on whether solar cells are used purely for energy harvesting, namely their conventional use, or for communication or for both uses simultaneously. The underlying reason for this is that the equivalent circuits differ depending on our purpose.

The DC model of a solar panel has been well-established for over 50 years [14]. The equivalent circuit of this single-diode model is illustrated below:

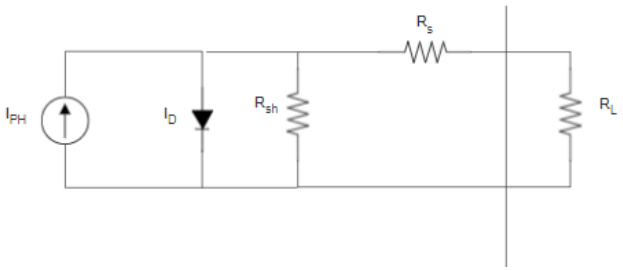

Figure 3: Equivalent circuit of the DC model for energy harvesting (left) and a resistive load for the bias of the solar cell (right)

The basic characteristics of this model are the photocurrent source I_{PH}, the diode which is connected in parallel to the source with current I_D, the shunt resistor R_{sh} that represents leakage current in the solar panel and the series resistance R_s that models the internal voltage loss due to the interconnections between cells as well as losses that occur in the

metallization of the cell. R_L is the resistive load across the solar cell which allows us to have control of the operating point of the cell. Following the above model, the I-V characteristic may be determined by the governing current equation for the single-diode model:

$$I = I_{ph} - I_D - I_{sh} \quad (1)$$

:

The shunt current is given by $I_{sh} = \frac{V+IR_s}{R_{sh}}$ (2)

where $V = R_L I$ (3), R_L being the resistance of the load across the solar cell.

The current of the diode can be obtained as:

$$I_d = I_o \left[\exp\left(\frac{V_d}{V_T}\right) - 1\right] \quad (4)$$

where the thermal voltage of the diode is $V_T = \frac{kAT}{q}$ (5)

A is the diode ideality factor, I_o the saturation current, V_D voltage across the diode, q the charge of an electron and k the Boltzmann constant. The diode ideality factor describes how close the slope of the *I-V* curve is to that of an ideal diode whose $n = 1$.

Substituting back into the equation for the shunt current and diode current, we obtain

$$I = I_{ph} - I_o \left[\exp\left(\frac{V+IR_s}{V_T}\right) - 1\right] - \frac{V+IR_s}{R_{sh}} \quad (6)$$

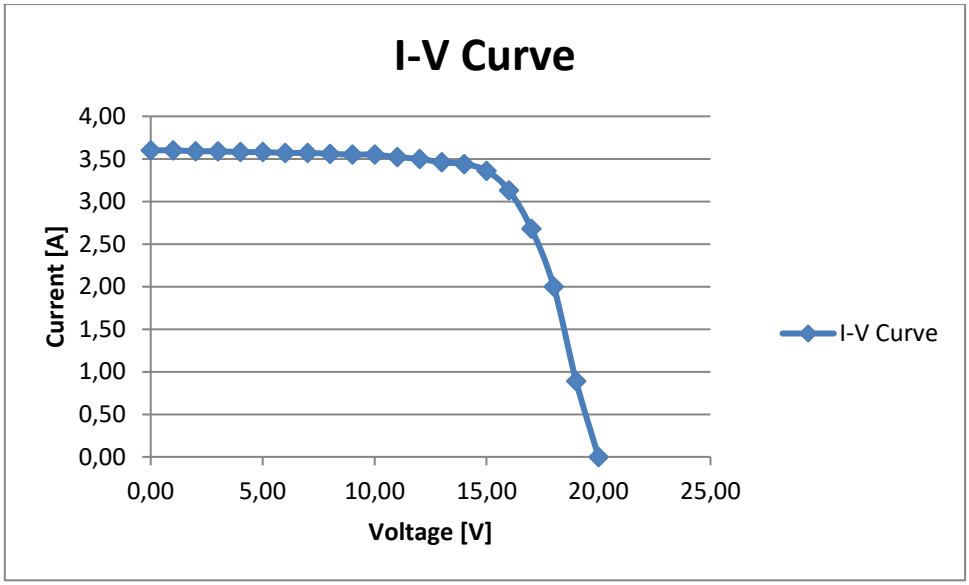

Figure 4: Example of an I-V curve obtained via DC model in MATLAB

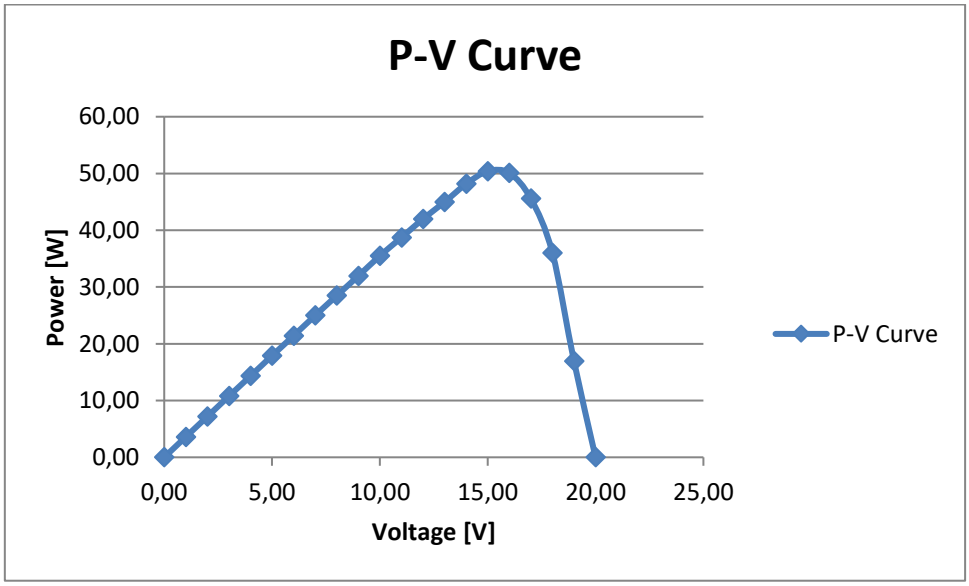

Figure 5: Example of a P-V curve obtained via DC model in MATLAB

We have not yet included temperature and irradiance effects on our DC model. Therefore, we also define the deviation from the standard temperature conditions of $T_n = 25°C$.

$$dT = T - T_n$$

and express the reverse saturation current as:

$$I_o = \frac{(I_{sc} + K_i \cdot dT)}{\exp\left[\frac{V_{OC} + K_V \cdot dT}{V_t} - 1\right]} \quad (7)$$

Additionally, the photo-current may be expressed in the following way which shows the effect of a different irradiance than $G_n = 1000 W/m^2$.

$$I_{PV} = (I_{sc} + K_i \cdot dT) \cdot \frac{G}{G_n} \quad (8)$$

As far as the parameters in (2) are concerned, the Boltzmann's constant k, the electron charge q and the temperature T are known, while Iph, Io, A, Rsh and Rs are unknown and they depend on the overall light irradiance of the solar panel.

2.2 PV Modelling for Communication

As far as using solar cells and panels for communication purposes, we need a model which includes the AC characteristics of the device. Therefore, we ought to modify the aforementioned model. As shown in figure 6,

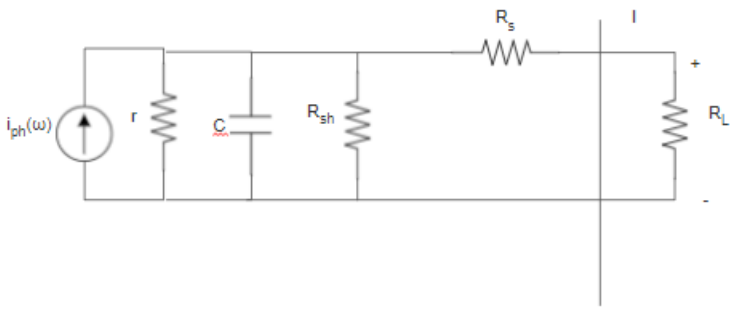

Fig. 6: AC small-signal model of a solar panel for communication purposes (left) and load across the solar cell (right)

$$\left|\frac{v(\omega)^2}{i_{PH}(\omega)}\right| = \left|\frac{\frac{R_L}{R_S + R_L}}{\frac{1}{r_d} + j\omega C + \frac{1}{R_{sh}} + \frac{1}{R_S + R_L}}\right| \quad (9)$$

to represent the AC behavior of the receiver, one may replace the forward-biased diode of the energy harvesting model (Figure 3), with its dynamic model which embeds a dynamic resistance and a dynamic capacitance (diffusion capacitance) [15]. We need the capacitance in order to capture the internal capacitive effects of the solar cell. Then to obtain equation 9 which is the transfer function, we use the current divider method with the impedance of each component in the circuit and convert current measured across the solar cell to frequency-dependent voltage v(ω). Then the transfer function is expressed as the ratio of v(ω) to the photogenerated current

2.2.1 Dynamic Resistance

Dynamic resistance is the resistance of a diode when an AC voltage or current is applied to it. The dynamic resistance may be obtained by calculating the partial derivative of the diode voltage versus the diode current at the operating point, using the Taylor's series expansion:

$$\boldsymbol{r_d = -\frac{\partial V_d}{\partial I_d}|_{O.P.}} \quad (10)$$

We may express the time-varying input voltage of the diode into the DC input voltage (called bias), which is determined by the operating point, plus the AC small-signal variation as follows:

$$v_{in}(t) = V_{in} + \widetilde{v_{in}(t)} \quad (11)$$

We may also express the diode current as follows:

$$i_d(t) = I_o\left(e^{\frac{v_{in}(t)}{V_t}} - 1\right) = I_d + \widetilde{i_d(t)} \quad (12)$$

The Taylor series generally dictates that:

$$f(x) = \sum_{n=0}^{\infty} \frac{1}{n!} \cdot \frac{d^n f(x)}{dx^n}|_{x=X} \cdot (x - X)^n = f(X) + \frac{df(x)}{dx}|_{x=X} \cdot (x - X)$$

Applying the Taylor expansion to the diode current around $V_{in,}$ we obtain

$$i_d\big(v_{in}(t)\big)|_{v=V_{in}} = i_d(V_{in}) + \frac{di_d(v_{in})}{dv_{in}}|_{v_{in}=V_{in}} \cdot (v_{in} - V_{in})$$

$$= I_o\left(e^{\frac{v_{in}(t)}{V_t}} - 1\right) + \frac{I_o}{V_t} \cdot e^{\frac{V_{in}}{V_t}}|_{v_{in}=V_{in}} \cdot (v_{in} - V_{in})$$

$$= I_o\left(e^{\frac{v_{in}(t)}{V_t}} - 1\right) + \frac{I_o}{V_t} \cdot e^{\frac{V_{in}}{V_t}}|_{v_{in}=V_{in}} \cdot \widetilde{v_{in}}$$

The first term is the DC component of the diode current and the second term is the small-signal AC current which may be expressed as:

$$I_d(V_{in}) + \frac{\widetilde{v_{in}}}{\frac{V_t}{I_o} \cdot e^{-\frac{V_{in}}{V_t}}}$$

The denominator of the second term, i.e. the AC current is the dynamic resistance, since

$$\widetilde{i_d(t)} = \frac{\widetilde{v_{in}}}{r_d} \quad (13)$$

Consequently,

$$\boldsymbol{r_d = -\frac{\partial V_d}{\partial I_d}|_{O.P.} = \frac{V_t}{I_o} \cdot e^{-\frac{V_{in}}{V_t}}} \quad (14)$$

From equation 14 we conclude that when the bias voltage is increased, dynamic resistance decreases, thus having a less significant contribution to the behavior of the cell toward the maximum power point and open-circuit conditions.

2.2.2. Dynamic Capacitance

The next component of the small signal model is the dynamic capacitance $\boldsymbol{C_d}$. As is the case with the dynamic resistance, the capacitance is dependent on the physical properties of the solar cell. For a given semiconductor, the dynamic capacitance is generally composed of the diffusion capacitance C_d, which is associated with the rearrangement of minority carrier density, as well as the junction capacitance C_j, which is associated with charge stored in the depletion region.

$$C = C_d + C_j \quad (15)$$

Specifically, the total capacitance of a solar cell takes into account the junction and free carrier capacitances. The latter is comprised mostly of the diffusion capacitance, namely the minority carrier storage in the quasi-neutral regions, and to a lesser extent the transient carrier capacitance attributed to defects and interface states [15].

When the junction is reverse-biased or has a small forward bias, the junction capacitance dominates. For more heavily forward-biased diodes, the diffusion capacitance contributes more significantly to the overall dynamic capacitance, as seen in figure 7. Consequently, the junction capacitance is negligible when we operate at maximum power point and open-circuit conditions. However, it should be taken into account when operating at short-circuit conditions. Finally, the transient capacitance only becomes noticeable when the bias voltage is extremely high [16].

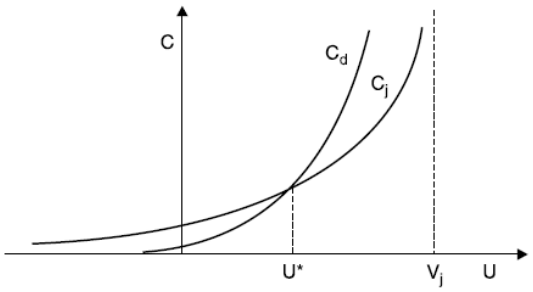

Figure 7: Variations of C_j and C_d with the bias voltage U [16]

Determining the diffusion capacitance is done as follows:

The diffusion capacitance may be calculated as

$$C_d = \frac{q}{kT} \cdot \tau(I_D + I_S) \quad (15)$$

where I_S is the saturation current, I_D is the diode current and τ is the minority carrier lifetime:

Additionally, the transition or junction capacitance may be calculated as [17]

$$C_j = \frac{\sqrt{\frac{\varepsilon_O \varepsilon_q \cdot N_A}{2V_j} \cdot S}}{(1-\frac{U}{V_j})^{1/2}} \quad (16)$$

Where C_{jo} is the zero-voltage junction capacitance, ε_O is the vacuum permittivity, ε_q is the charge permittivity, S is the diode surface area, N_A is the semiconductor acceptor concentration, V_j is the built-in voltage and U is the bias voltage.

Other than the bias voltage, factors affecting solar cell capacitance, albeit the effect is relatively minor, are the level of irradiance as well as the frequency of the incident signal [11]. Specifically, figure 8 shows that as the level of irradiance increases, solar cell capacitance increases by a small amount. Additionally, as the frequency of the incident signal increases, capacitance decreases at a rather slow rate [10]; Kumar et al found about a 1% reduction of the capacitance value from 10kHz to 56kHz.

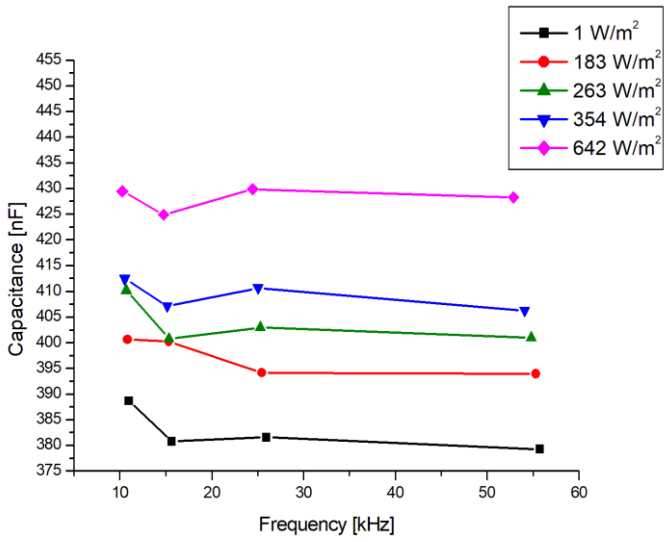

Figure 8: Irradiance and frequency effects on solar cell capacitance [17]

Finally, temperature has an effect on solar cell capacitance that may be approximated by a fourth-degree polynomial. As temperature increases, solar cell capacitance increases [18].

The AC equivalent circuit for communication in figure 6 depicts AC voltage measurements across the load. When the load across the cell is high, we operate in open-circuit. In the short-circuit case, the load across the cell is low (or zero ideally). Hence, we can use the model for all operating conditions.

The inductor L is added to the circuit in figure 9 to model the inductance of any wire connections to the solar cell. Only the AC component of the photocurrent $i_{PH}(\omega)$ is used for communication. Also, a capacitor C_o is added before the resistor R_C to block the DC component of the signal. The information signal is represented by the voltage or current across the resistive load R_C. It is important to note that for the purposes of our modeling the shunt and series resistance do not change with irradiance.

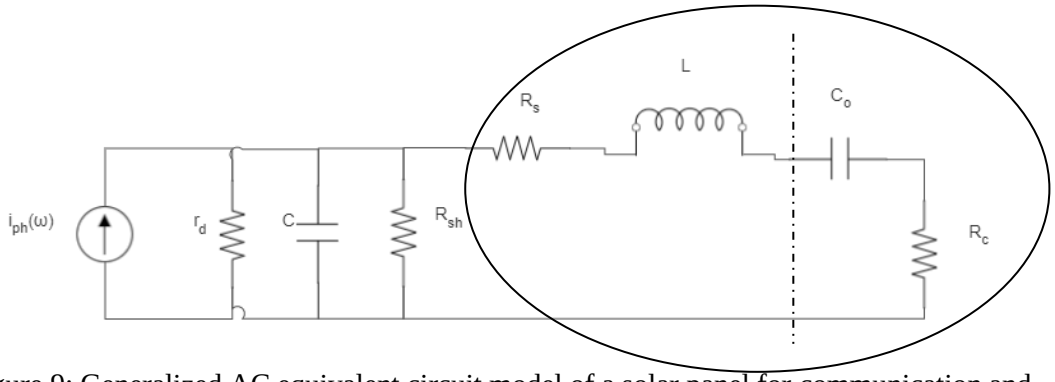

Figure 9: Generalized AC equivalent circuit model of a solar panel for communication and RC filter across the cell [6]

The frequency response of the solar panel configuration for communication is expressed as [6]:

$$\frac{v(\omega)}{i_{PH}(\omega)} = \frac{\frac{R_C}{R_X}}{\frac{1}{r_d} + j\omega C + \frac{1}{R_{sh}} + \frac{1}{R_X}} \quad (17)$$

where v(ω) is the voltage across Rc and

R_X (circled in figure 11) is the resistance that is parallel with the shunt resistance and is determined by adding all the individual impedance components:

$$R_X = R_S + j\omega L + \frac{1}{j\omega C_0} + R_C$$

Equation 17 allows us to simulate the solar cell in frequency-domain where the angular frequency $\omega = 2\pi f$.

2.3 PV Modelling for Simultaneous Energy Harvesting & Communication

Our ultimate goal is to model the simultaneous use of a solar panel both for harvesting energy and for communication. Therefore, certain modifications are required in the AC equivalent circuit shown in figure 10, in order to achieve both purposes. The equivalent circuit is illustrated below:

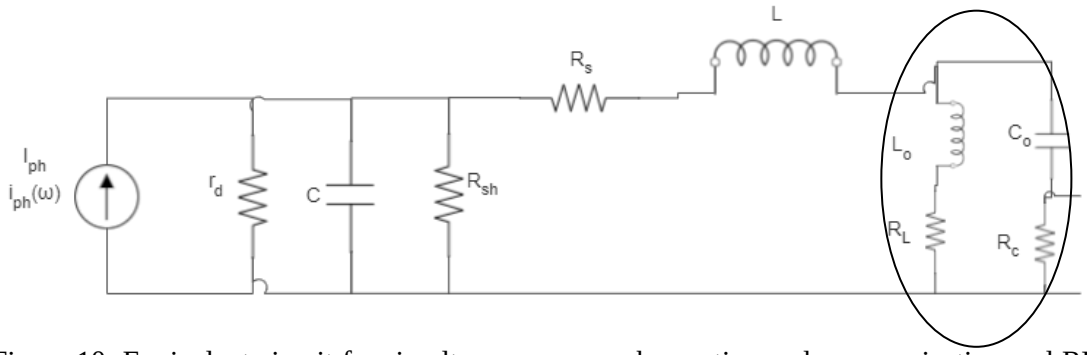

Figure 10: Equivalent circuit for simultaneous energy harvesting and communication and RL and RC filters across the solar cell[6]

The resistor R_C and the capacitor C_o form the communication branch. An extra branch is added for energy harvesting in parallel with the branch for communication. That energy harvesting branch includes a resistor $R_L$and an inductor L_o. The inductance attenuates the AC signal, by blocking the high-frequencies. The inductor $L_o$and the capacitor C_o affect the DC value and ensure that the DC signal is not entangled with the AC signal in a way that the DC signal passes through the RL branch and the AC signal through the RC branch. The resistor R_L defines our operating point. A small R_L makes us operate close to short-circuit and a high R_L closer to open-circuit.

The behavior of solar cells in VLC is that of a low pass filter. This filter may be single pole or double pole. The pole is defined by the dynamic resistance r_d and capacitance C.

The frequency response of the equivalent circuit model in Figure 10 is determined to be :

$$\frac{v(\omega)}{i_{PH}(\omega)} = \frac{\frac{R_{LC}}{R_S+j\omega L+R_{LC}} \cdot \frac{R_C}{\frac{1}{j\omega C_O+R_C}}}{\frac{1}{r}+\frac{1}{j\omega C}+\frac{1}{R_{sh}}+\frac{1}{R_S+j\omega L+R_{LC}}} \quad (18)$$

R_{LC} is the impedance of the parallel RL and RC branches circled in Figure 10:

and may be determined by adding the impedance of the series components in each branch and adding them in parallel.

$$R_{LC} = \frac{1}{\frac{1}{j\omega L_O+R_L}+\frac{1}{\frac{1}{j\omega C_O}+R_C}} \quad (19)$$

We need to bear in mind that Lo and R_L are relatively large in comparison to 1/Co and Rc, so that the AC component passes through to the communication branch.

The above proposed model works in all operating points and communication frequencies. For instance, let us assume a low frequency. In this case, the capacitor C_o would operate as in open-circuit and the inductor L_o in short-circuit. On the other hand, in high frequency, the capacitor C_o would operate as in short-circuit and the inductor L_o as in open-circuit.

The effect the resistor R_C of the communication branch is the following: as the value of R_C increases, the overall gain of the frequency response increases and the corresponding 3-dB bandwidth decreases [6].

To comprehend the experimental results we obtained (presented in chapter 4) for the frequency domain and relate them to our modelling, we introduce a concept called the gain. Gain is the ratio of the output voltage or current to the input voltage or current expressed in logarithmic units (dB). In higher frequencies, the gain starts to decrease. The 3-dB bandwidth is the frequency for which we have a -3dB gain with reference to the DC value, which is at zero frequency.

$$\text{Voltage Gain } G[dB] = -20\log\left(\frac{V_{out}}{V_{in}}\right) \quad (20a)$$

We may also express the current gain as

$$\text{Current Gain } G[dB] = -20\log\left(\frac{I_{out}}{I_{in}}\right) \quad (20b)$$

The output current or voltage is measured across the solar cell (e.g. $v(\omega)$ in equation 18) and the input is the photogenerated current $i_{PH}(\omega)$.

2.4 Filter design methodology

Cut-off frequency is the value of frequency in a frequency response where a signal is reduced at 70% compared to its initial value at low frequencies. The signal in our case can be either voltage or current measured at the solar cell. In order to accurately provide a concrete recommendation for the components of the 2-branch model (Equation 18), we use the experimental results obtained for cutoff frequency of the solar cells and design the RL and RC filters, so that an appropriate splitting of the AC and DC signal is achieved. RL is a low-pass filter and RC is a high-pass filter.

For the RC component of the circuit we obtain the values for RC as follows. The cutoff frequency is computed as:

$$f_C = \frac{1}{2\pi R_c C_o} \quad (21)$$

For the RL branch we obtain the values for RL as follows:

The cutoff frequency is computed as

$$f_L = \frac{R_L}{2\pi L_o} \quad (22)$$

The range of values of our load for all measured operating points

$$0.013\Omega \leq R_l \leq 0.68\Omega$$

For the low pass RL filter holds: $f_L = \frac{R_L}{2\pi L_o}$

Hence, the range of values for the inductor in the energy harvesting branch is determined in Chapter 5.

Additionally,

$$f_C = \frac{1}{2\pi \cdot R_c C_o}$$

Thus, the range of values of our capacitor in the communication branch is determined in Chapter 5, where we use this filter design approach.

The 2-branch model yields frequency response curves that are the result of a low-pass filter, i.e. the cell, the RL low-pass filter and the RC high-pass filter. We assume that the inductor of the energy harvesting branch does not influence the operating point of the cell. This is certainly true for low measurements and is an acceptable assumption for the range of frequencies of the obtained measurements.

3. EXPERIMENT

3.1 Experimental setup analysis

Using photovoltaics in visible light communication is a relatively nascent field. There are several papers which describe the use of solar cells as receivers. Conversely, there is limited data using photovoltaics for transmission. Currently, the only successful prototype was created by the LiFi Research and Development Centre at the University of Edinburgh in March 2020. Harald Haas' group showed that it is possbile for a solar cell to operate a light fidelity transmission under additional solar illumination in open-circuit conditions [4]. We utilize solar cells as VLC receivers.

Even more importantly, when utilizing an outdoor setup to obtain measurements, we encounter variable ambient conditions, such as temperature and light intensity, which we cannot control. This makes it hard to distinguish which measurements should be taken into account and which are simply the result of these variable conditions. Consequently, we opted for an indoor laboratory setup to have control over the environment and observe trends attributable to other factors. Such a setup would allow us to obtain real experimental results by simulating the solar illumination with a light source that would yield close to $1000W/m^2$ to approximate standard test conditions. Additionally, our aim is to charaterize solar cells for different levels of light intensity, AC signal and resistive load across them.

During the first part of our experimental work, we used a customized LED matrix consisting of 16 LED strips for VLC transmission, shown in figure 11. The distance between two LED strips in the matrix is 2.5 cm. Each strip has 15 LEDs and there are 16 LED strips for a total of 240 LEDs.

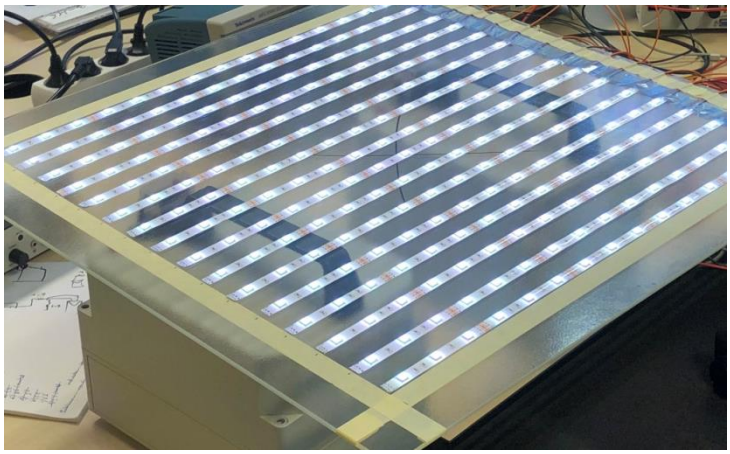

Figure 11: LED matrix

However, due to the fact that the LED matrix light intensity is insufficient, we decided to use a different light source (an LED) as a transmitter for the rest of our experimental data. The LED matrix intensity is also not uniformly distributed to the solar cell due to their comparatively low cell surface area.

On the transmitter side, we have an LED source which transmits a sinusoidal signal, using a digital Function Generator (Digilent Waveforms software). The LED spectrum is limited to 380nm to 840nm. We took measurements using the LED on its own with no lens, as well as some additional measurements using two different lenses (60^o and 120^o) mounted on the LED. The motivation behind using different LED lenses was to be able to increase the transmission light intensity and change its distribution across the custom grid (Figure 14). The waveforms software allows us to create a frequency sweep from 1Hz to 1MHz to observe how the voltage or current gain changes with frequency, i.e. the behavior or solar cells in frequency domain.

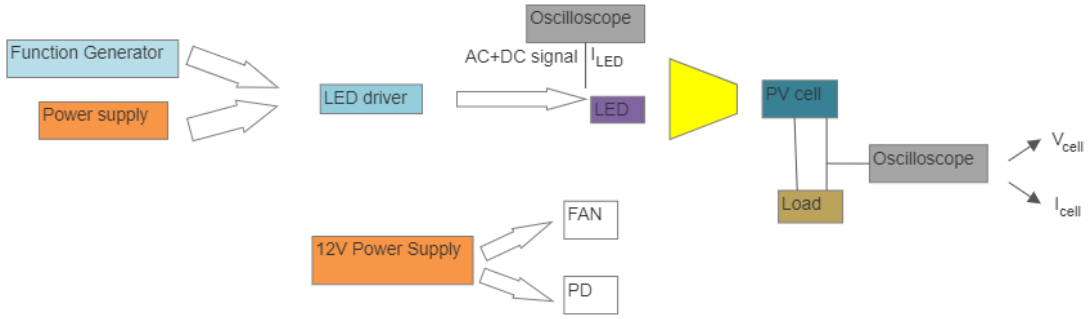

Figure 12: Block diagram of the experimental setup

On the receiver side, we utilized three solar cells: one monocrystalline silicon Front-Back Contacted (FBC) Aluminum Back Surface Field (Al-BSF) solar cells [29], one monocrystalline silicon FBC passivated emitter and rear contact (PERC) cell and one monocrystalline silicon Interdigitated Back Contact (IBC) cell [30]. The oscilloscope model we used on the cell was Digilent Analog Discovery 2 [34].

Cell Technology	**FBC, Al-BSF**	**FBC, PERC**	**IBC**
Surface Area (cm^2)	153	246	153
V_{oc} (V)	0.628	0.654	0.677
I_{sc} (A)	5.67	9.61	6.33
J_{sc} (mA/cm^2)	37.1	39.1	41.4
I_{mpp}	5.29	9.05	5.98
V_{mpp}	0.527	0.547	0.575
η (%)	18.0	20.4	22.4
FF (%)	78.3	78.8	80.2

Table 1: Solar cell data of cells as VLC receivers

For mounting the light source and being able to control the distance between the LED and the solar cell, we utilized a frame with an adjustable component that we were able to move along to adjust the height/link distance, as seen in Figure 13:

Figure 13: Frame structure of experimental setup

3.2 Experimental setup characterization

3.2.1 LED transmission light intensity

We measured the LED light intensity using a photodiode and an Oscilloscope Agilent current probe with sensitivity 100mV/A on a custom-made grid which allowed us to understand how light intesity is distributed across a given surface area. The grid was split into 8 columns and 9 rows, with even segments. Measurements were conducted in a dark room. We also ensured that there was minimal to no tilted angle between the LED and the diode using a thin piece of carton to prop up the base of the photodiode. After obtaining all the light intensity values for all positions across the grid, we changed the height of the LED in the frame, thus varying the link distance. Consequently, we were able to observe how increasing or decreasing the link distance affected the performance of the solar cell.

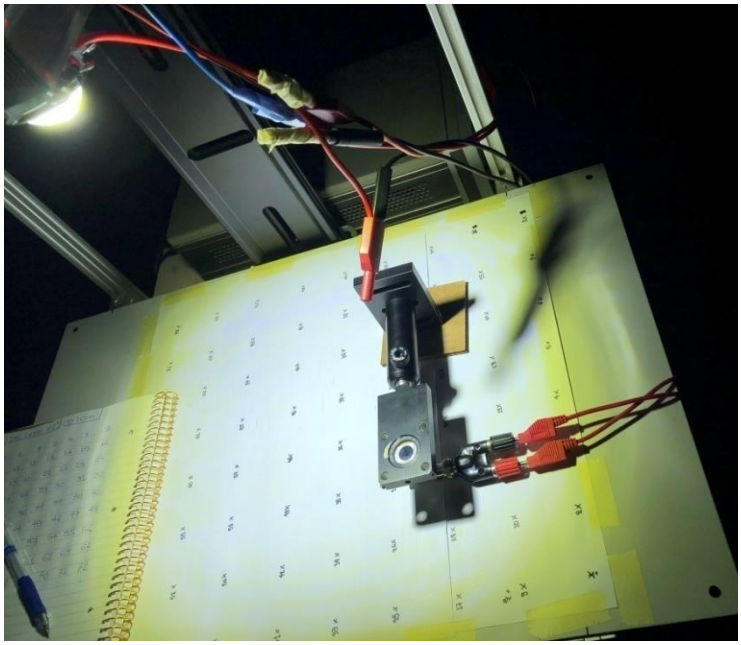

Figure 14: LED characterization using a Photodiode (PD)

Position	**1**	**2**	**3**	**4**	**5**	**6**	**7**	**8**
Current [µA]	628	661	686	697	703	691	677	650
	9	**10**	**11**	**12**	**13**	**14**	**15**	**16**
	648	694	718	737	742	738	728	698
	17	**18**	**19**	**20**	**21**	**22**	**23**	**24**
	704	740	763	777	775	762	734	700
	25	**26**	**27**	**28**	**29**	**30**	**31**	**32**
	719	758	783	790	793	789	771	736
	33	**34**	**35**	**36**	**37**	**38**	**39**	**40**
	724	760	787	804	802	796	778	748
	41	**42**	**43**	**44**	**45**	**46**	**47**	**48**
	720	759	786	803	806	810	806	795
	49	**50**	**51**	**52**	**53**	**54**	**55**	**56**
	701	743	767	785	796	792	785	784
	57	**58**	**59**	**60**	**61**	**62**	**63**	**64**
	671	708	736	752	758	759	759	702
	65	**66**	**67**	**68**	**69**	**70**	**71**	**72**
	635	663	686	696	707	696	686	662

Table 2: LED light intensity at 65cm link distance with no lens

By decreasing the link distance to 30cm, we obtained the following results:

Position	**1**	**2**	**3**	**4**	**5**	**6**	**7**	**8**
Current [μA]	1225	1481	1728	1881	1951	1794	1713	1440
	9	**10**	**11**	**12**	**13**	**14**	**15**	**16**
	1522	1930	2213	2346	2437	2281	2175	1780
	17	**18**	**19**	**20**	**21**	**22**	**23**	**24**
	1850	2337	2676	2980	3031	2934	2638	2182
	25	**26**	**27**	**28**	**29**	**30**	**31**	**32**
	2002	2534	3038	3365	3517	3309	2978	2525
	33	**34**	**35**	**36**	**37**	**38**	**39**	**40**
	2112	2691	3224	3638	3716	3521	3164	2615
	41	**42**	**43**	**44**	**45**	**46**	**47**	**48**
	2074	2635	3238	3618	3672	3545	3153	2640
	49	**50**	**51**	**52**	**53**	**54**	**55**	**56**
	1937	2446	2911	3213	3313	3172	2896	2416
	57	**58**	**59**	**60**	**61**	**62**	**63**	**64**
	1696	2051	2421	2673	2758	2684	2385	2027
	65	**66**	**67**	**68**	**69**	**70**	**71**	**72**
	1389	1665	1957	2073	2168	2062	1904	1615

Table 3: LED light intensity at 30cm link distance with no lens

Position	**1**	**2**	**3**	**4**	**5**	**6**	**7**	**8**
Current [μA]	251	549	813	968	985	1000	751	432
	9	**10**	**11**	**12**	**13**	**14**	**15**	**16**
	558	1611	3547	4420	4657	2414	2660	828
	17	**18**	**19**	**20**	**21**	**22**	**23**	**24**
	1246	4304	6638	7597	7771	7057	5723	2997
	25	**26**	**27**	**28**	**29**	**30**	**31**	**32**
	1503	5391	7895	8921	9093	8469	7011	4464
	33	**34**	**35**	**36**	**37**	**38**	**39**	**40**
	1939	5915	8643	9659	9944	9186	7614	4362
	41	**42**	**43**	**44**	**45**	**46**	**47**	**48**
	2013	5744	8219	9483	9691	9060	7768	4985
	49	**50**	**51**	**52**	**53**	**54**	**55**	**56**
	1509	5002	7148	8161	8424	7839	6843	4759
	57	**58**	**59**	**60**	**61**	**62**	**63**	**64**
	977	2824	4693	5362	5683	5195	4163	1873
	65	**66**	**67**	**68**	**69**	**70**	**71**	**72**
	382	905	1350	1852	2096	1637	1195	519

Table 4: LED light intensity at 30cm link distance with 60^o lens

From tables 2 and 3, we observe that decreasing the link distance in half leads to about a 3-fold increase in light intensity which varies depending on where we measured across the grid. Increases in light intensity were proportionally higher at the center.

Position	**1**	**2**	**3**	**4**	**5**	**6**	**7**	**8**
Current [μA]	1330	2137	2680	3005	3026	2571	1775	635
	9	**10**	**11**	**12**	**13**	**14**	**15**	**16**
	2037	3022	3913	4398	4439	3936	1835	1089
	17	**18**	**19**	**20**	**21**	**22**	**23**	**24**
	3065	4256	5187	5944	6105	5445	4421	2873
	25	**26**	**27**	**28**	**29**	**30**	**31**	**32**
	3656	5108	6362	7224	7251	6557	5101	3622
	33	**34**	**35**	**36**	**37**	**38**	**39**	**40**
	3958	5556	6966	7983	8058	7184	5619	4140
	41	**42**	**43**	**44**	**45**	**46**	**47**	**48**
	3767	5087	6657	7848	7960	7200	5757	4268
	49	**50**	**51**	**52**	**53**	**54**	**55**	**56**
	3327	4589	5769	6550	6742	6069	5132	3740
	57	**58**	**59**	**60**	**61**	**62**	**63**	**64**
	2585	3444	4358	4854	4941	4575	3894	2668
	65	**66**	**67**	**68**	**69**	**70**	**71**	**72**
	1716	2505	3151	3512	3980	3205	2666	1818

Table 5: LED light intensity at 30cm link distance with 120^o lens

A comparison of the results we obtain for different lenses, while keeping link distance constant leads to the conclusion that both lenses leads to increases in light intensity at the center of the grid while reduced intensity is obtained as we move toward grid points further away from the center. The 120^o lens indicates the highest increase in the center of the grid compared to the 60^o lens and no lens, with the sharpest drop in light intensity toward the edge of the grid.

The values we obtained in the LED characterization were in μA, which we then standardized (multiplied by 46800/6500) to convert to Lux. For instance, table 6 in Lux:

Position	**1**	**2**	**3**	**4**	**5**	**6**	**7**	**8**
Light Intensity [Lux]	9576	15386	19296	21636	21787	18511	12780	4572
	9	**10**	**11**	**12**	**13**	**14**	**15**	**16**
	14666	21758	28174	31666	31961	28339	13212	7841
	17	**18**	**19**	**20**	**21**	**22**	**23**	**24**
	22068	30643	37346	42797	43956	39204	31831	20686
	25	**26**	**27**	**28**	**29**	**30**	**31**	**32**

	26323	36778	45806	52013	52207	47210	36727	26078
	33	**34**	**35**	**36**	**37**	**38**	**39**	**40**
	28498	40003	50155	57478	58018	51725	40457	29808
	41	**42**	**43**	**44**	**45**	**46**	**47**	**48**
	27122	36626	47930	56506	57312	51840	41450	30730
	49	**50**	**51**	**52**	**53**	**54**	**55**	**56**
	23954	33041	41537	47160	48542	43697	36950	26928
	57	**58**	**59**	**60**	**61**	**62**	**63**	**64**
	18612	24797	31378	34949	35575	32940	28037	19210
	65	**66**	**67**	**68**	**69**	**70**	**71**	**72**
	12355	18036	22687	25286	28656	23076	19195	13090

Table 6: LED light intensity at 30cm link distance with 120^o lens in Lux

Finally, we are able to convert these measurements in W/m^2. In the visible part of the spectrum, according to the IEEE conversion guide 1000W/m^2 is equal to 120,000 Lux [35].

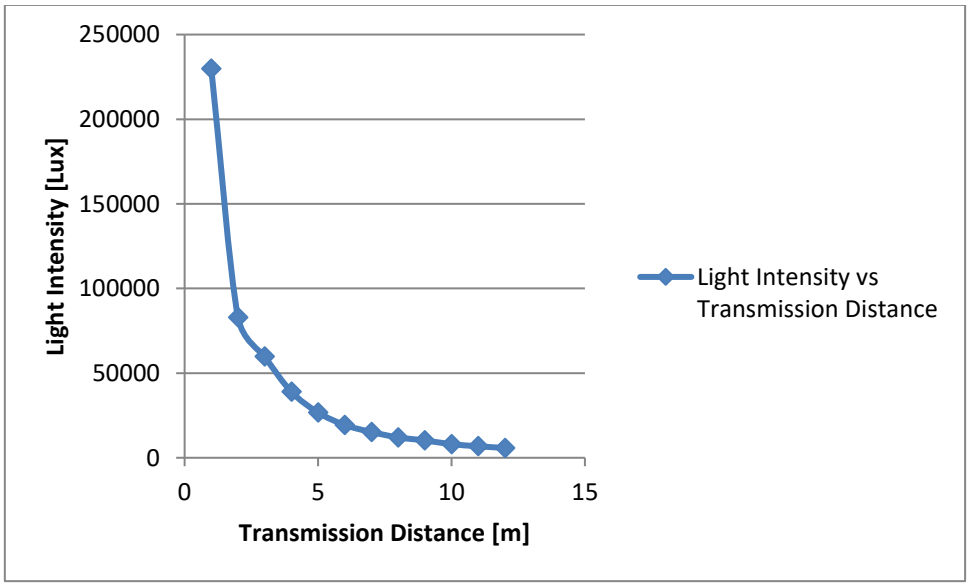

Figure 15: Light Intensity vs. Transmission Distance for vertical alignment of LED with no added lens and Receiver at position 45 (center)

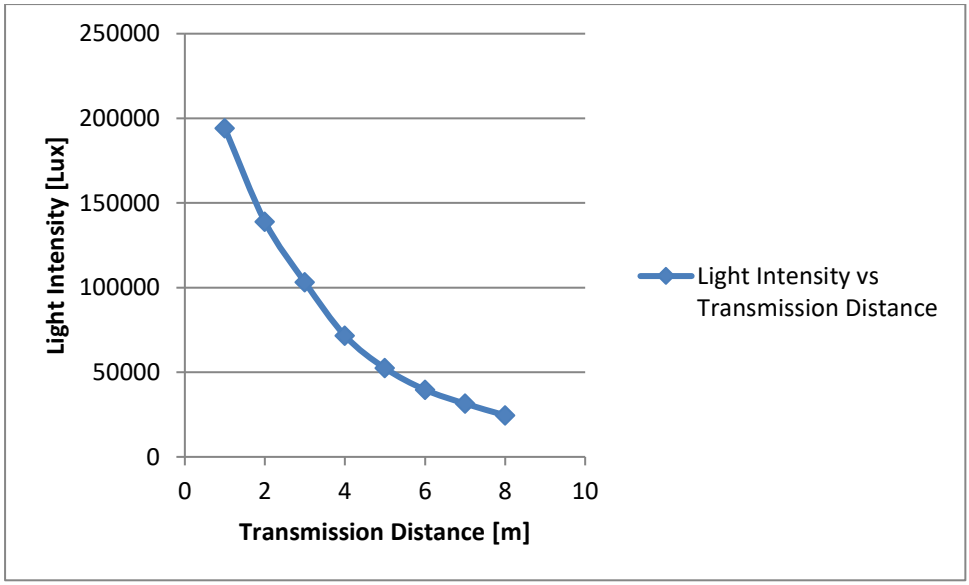

Figure 16: Light Intensity vs. Transmission Distance for vertical alignment of LED with 60^o lens and Receiver at position 45 (center)

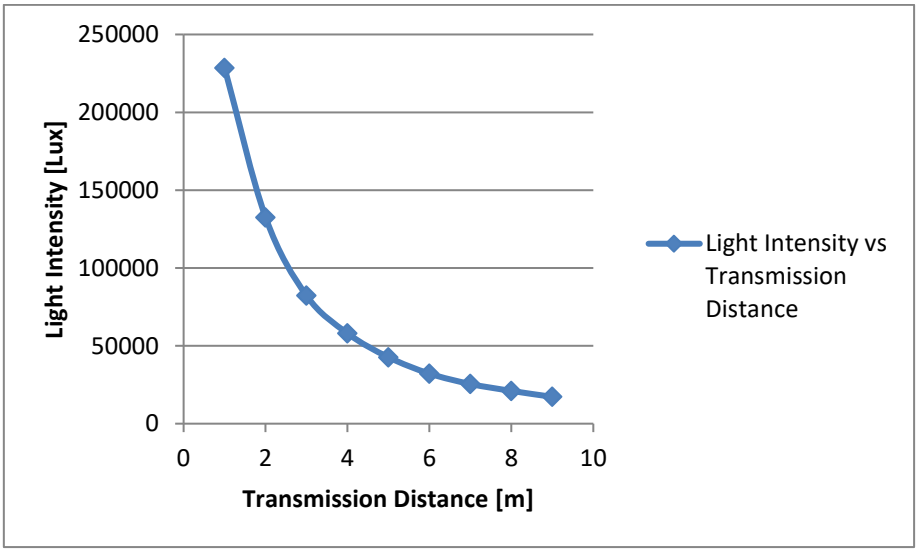

Figure 17: Light Intensity vs. Transmission Distance for vertical alignment of LED with 120^o lens and Receiver at position 45 (center)

We conclude that in order to approximate the level of solar irradiance at 1000W/m^2, the 120^o lens is recommended. Specifically, a 10 cm link distance should be set and the receiver centered at position 45, namely the center of the grid.

3.3 Experiments

For our initial set of measurements, we used the LED strips as transmitter sending a square signal. However, the light intensity of the matrix was not sufficient. As a result, the current obtained as an output is too low for proper measurements.

For the second set of measuremets, we used a 100W LED with spectrum similar to that of the sun, i.e. 380nm to 840nm, with 32V and 3.5A input voltage and current. The 32V voltage is the maximum voltage supported by our LED. Our function generator cannot handle a sufficiently high current to drive the LED transmission. Therefore, we need the power driver. It is also worth noting that the bandwidth of our LED driver was around 65kHz which is higher than the bandwidth of the solar cells meaning that it had not influence on the results.

In addition, we need to send a sinusoidal signal to the LED without it switching off. Hence, the maximum value of our signal is 32V. Also, in order to achieve sinusoidal light intensity, we need a minimum voltage that is higher than the forward voltage of the LED. Below that minimum voltage, the LED would again switch off at the bottom half of the sinusoidal signal. To solve this problem, an op-amp was used., to be able to generate a signal with a peak-to-peak voltage of more than 10V, we used a gain and offset.

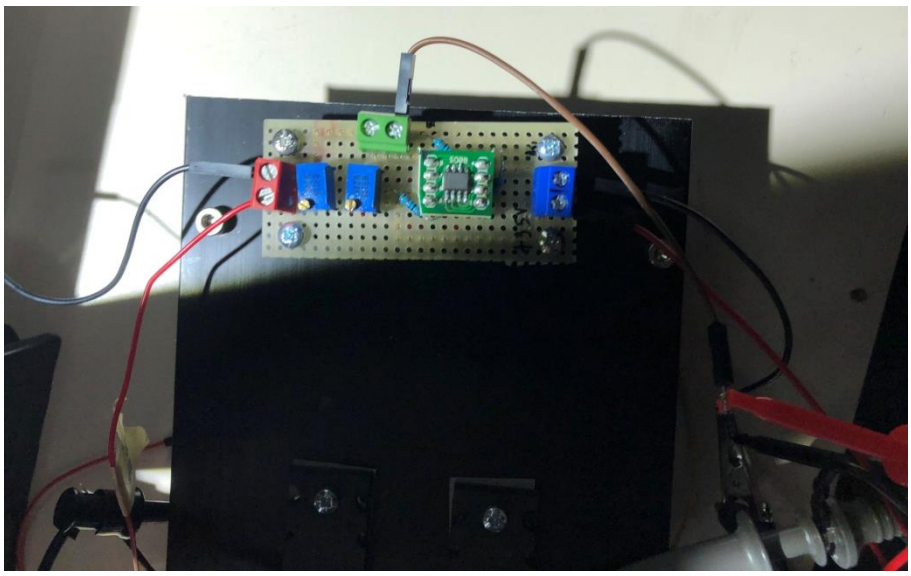

Figure 18: LED driver

There are several quantities both on the transmitter and on the receiver side that we vary. To begin with, we conducted measurements for various resistive loads, from nearly zero in order to be as close to short-circuit as possible(13mΩ), to 680mΩ thus being close to open-circuit. An attempt was made to operate the cell at exactly the maximum power point. In order to achieve this, we would have to use an active load. However, this is not feasible since the dynamic characteristics of the active load would influence our results. We also use different lenses (no lens, 60^o lens and 120^o lens), the light intensity is distributed differently across the surface area of the receiver and also amplified. Thirdly, we vary the link distance, i.e. the distance between the LED and the solar cell. Overall, we obtained data for all the aforementioned combinations of variables.

4. RESULTS

4.1 Experimental Results

The data presented in this chapter do not include the data utilizing the LED strips as transmitter; those have been discarded due to insufficient light intensity. We consider that the second set of data we obtained, using the LED instead of the LED strips, can be used for further study and fitting with our theoretical model.

The network analyzer data from Diligent Waveforms software shows that the frequency response of the IBC compared to the FBC cell, the IBC has a sharper drop towards the higher frequencies, but due to its higher capacitance the it indicates a higher dBV For Vin = 9.6V, use Waveform generator at 1.5V amplitude and 1V offset (for both Mono c-Si cells). For IBC: Vin = 9.4V, use amplitude of 2V and offset of 1.7V. The Oscilloscope Agilent Current Probe set at sensitivity of 100mV/A.

In the figures of the collected experimental data, the 0dB refrence for the current gain is the maximum PV current amplitude at a frequency of 100Hz.

Figure 21 shows the frequency response for the 5-inch FBC and IBC cells, as well as the cut-off frequency derived from that data with different load.

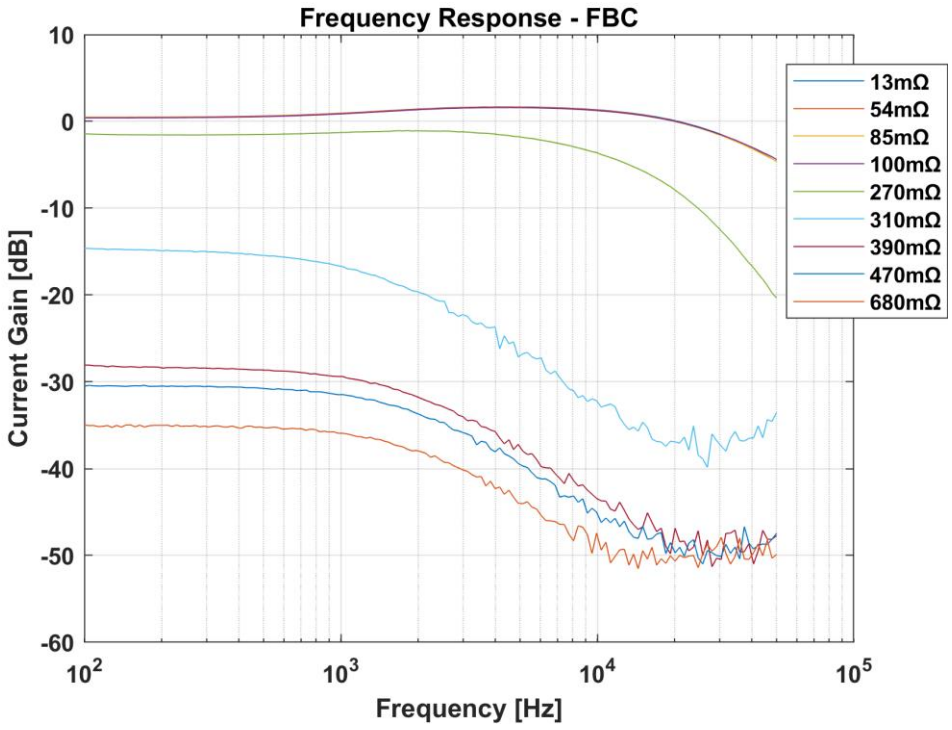

Figure 19: Frequency response curves for the 5-inch FBC cell at different loads

We notice that for loads up to 100mΩ, the frequency response curves indicate a "bump", i.e. a positive increase in gain. However, in our experimental setup that is described by the model in 4.2.1, which does not include an RC branch designed to optimize communication as is the case for the 2-branch model, this increase in gain is not theoretically predicted. One possible cause for this positive increase in gain is other capacitive/inductive effects of the solar cell or arbitrary parasitic effect of our setup.

Additionally, we notice that as we move towards the higher loads, the cutoff frequency is lower implying hindered communication. From figure 19, we also derived the following cutoff frequencies for the 5-inch FBC solar cell:

Load (mΩ)	Fc(kHz)
13, 54, 85, 100	37.41
270	12.23
310	1.65
390	1.74
470	1.89
680	1.96

Table 7: Cutoff-frequencies for the 5-inch FBC cell at different operating points

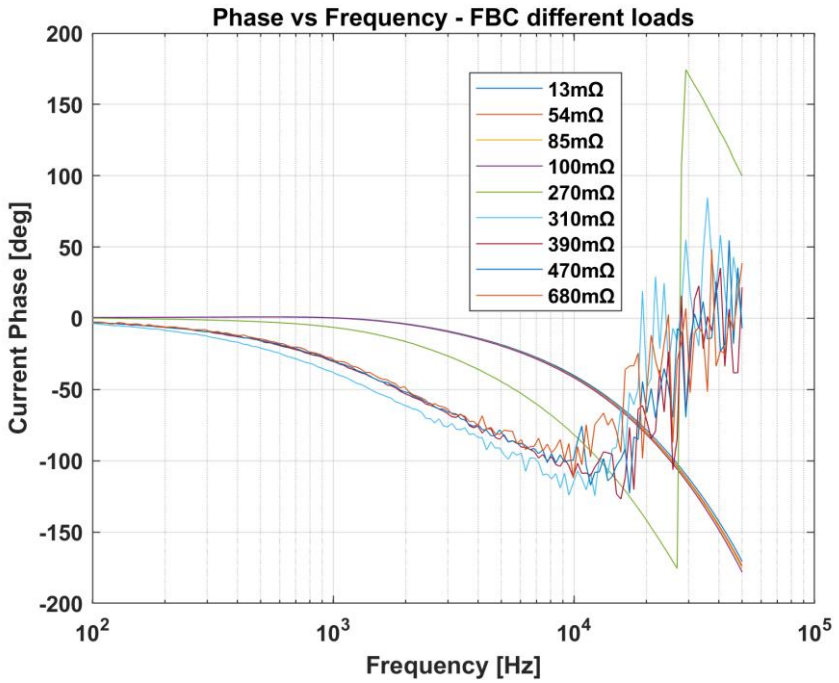

Figure 20: Phase vs Frequency curves for the FBC cell at different loads

The current phase in frequency domain of figure 20 depicts similarities between the very small loads up to 100mΩ with each other and for loads 310mΩ and above with

each other. Higher load measurements are also noisier at frequencies exceeding 10 kHz, so we do not take them into account. The phase shift starts to appear in higher frequencies for small loads. We also observe in figure 20 that at low load phase drops to 180^{o} whereas at higher loads it stabilizes around 90^{o}. The drop to 180^{o} and sharp increase subsequently may indicate a second order pole in our system. It is unclear whether a parasitic effect of our setup or the solar cell itself leads to this behavior.

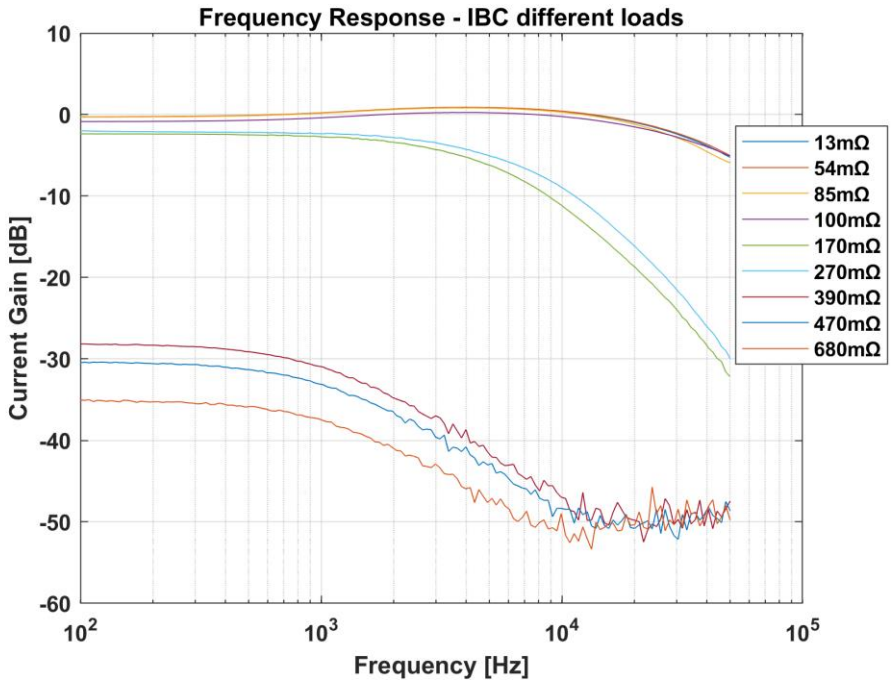

Figure 21: Frequency response curves for the IBC cell at different loads

Regarding the frequency response of the IBC cell, we observe a drop in current gain at lower frequencies compared to the FBC, thus lower cutoff frequencies. This confirms the lower achievable bandwidth of IBC cells for communication purposes. The "bump" in small loads appears again. Our system is underdamped at small loads. At loads of 170mΩ and 270mΩ the slope is higher compared to the smaller loads. Combined with the phase behavior of figure 22 similar to that discussed in figure 20, namely a drop to 180^{o} and a sharp increase, it is indicative of a second order pole.

Load (mΩ)	Fc(kHz)
13, 54, 85	27.99
100	25.77
170	5.12
270	4.16
390	1.06
470	1.10
680	1.06

Table 8: Cutoff-frequencies for the IBC cell at different operating points

In table 8, we notice a significant reduction in the IBC cell cut-off frequency especially towards the higher loads, i.e. the Maximum Power Point and Open-circuit. As already discussed, this is to be expected. The higher capacitance present in higher loads is linked with a lower cut-off frequency, thus limited bandwidth.

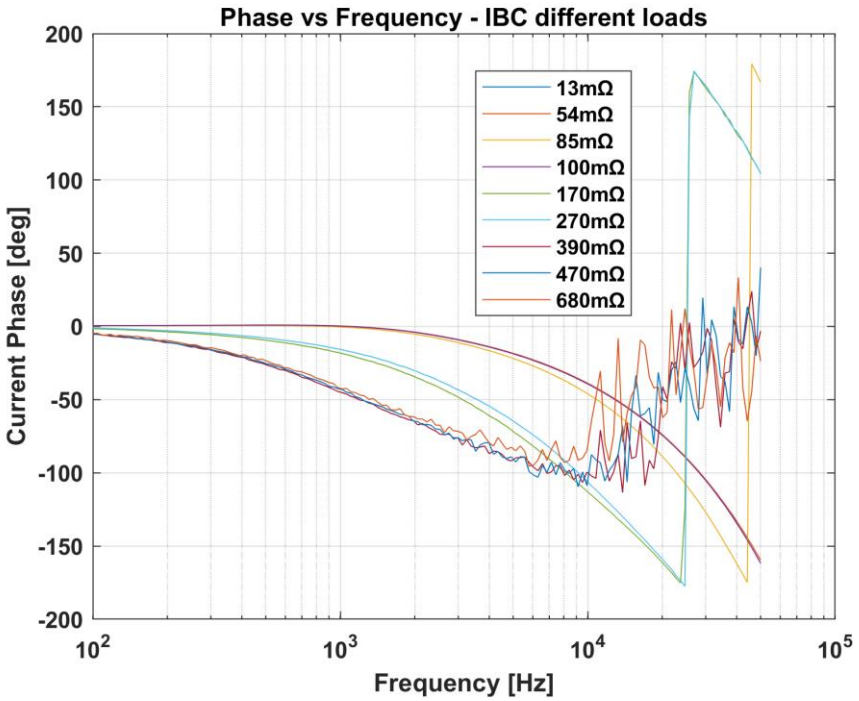

Figure 22: Phase vs Frequency curves for the IBC cell at different loads

Figure 22 shows the phase shift between the input current and the current measured at the solar cell. As the load increases, we notice this phase shift present itself at lower frequencies. We may now compare the two different types of cell at the same load and notice that the same load implies a different operating point, as well as different inherent capacitance.

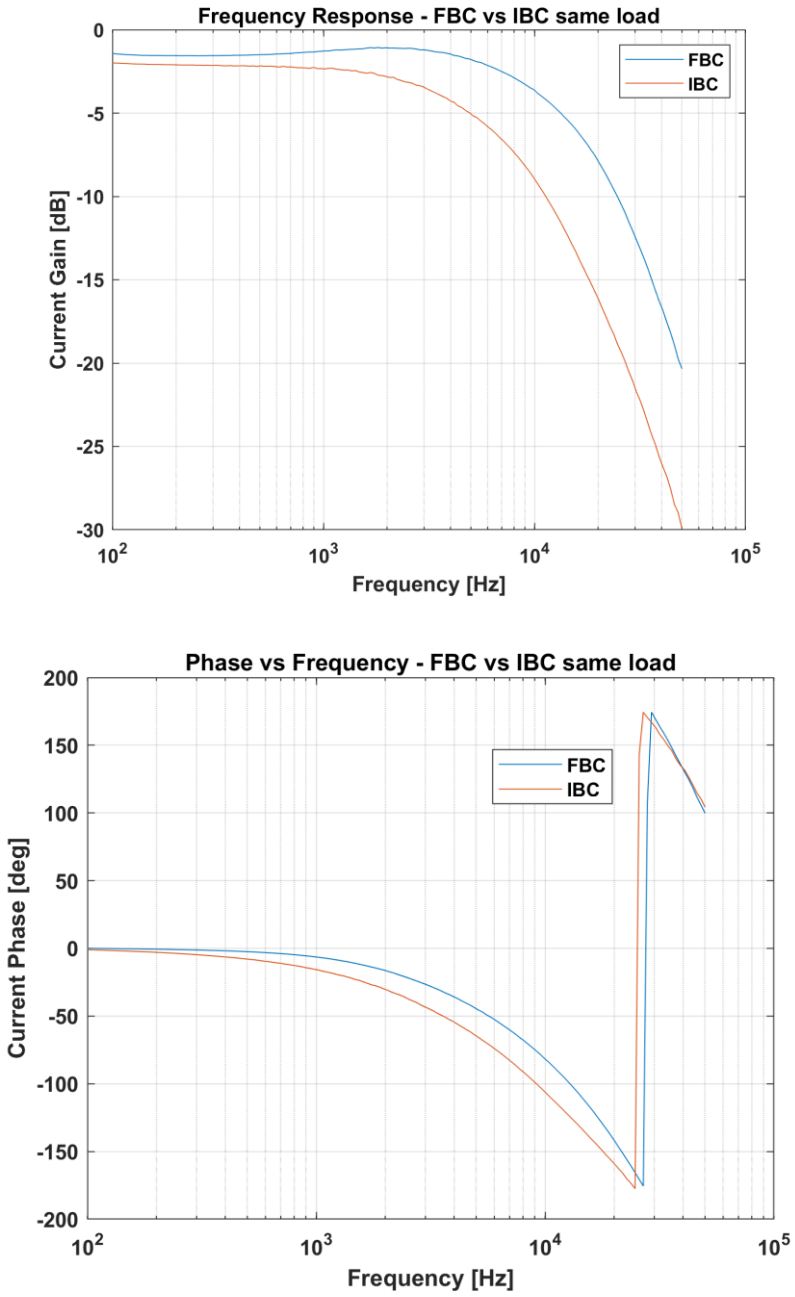

Figure 23: FBC vs IBC cell Current Gain & Phase vs. Frequency – Same Load 270mΩ

It is evident in figure 23 that the IBC cell indicates a drop in current gain at a lower frequency, which once again verifies the inherent tradeoff between communication bandwidth and energy harvesting due to its higher capacitance. In figure 23, we observe that there is a phase shift starting to occur at frequencies greater than 1kHz between the input current and the current measured at the cell.

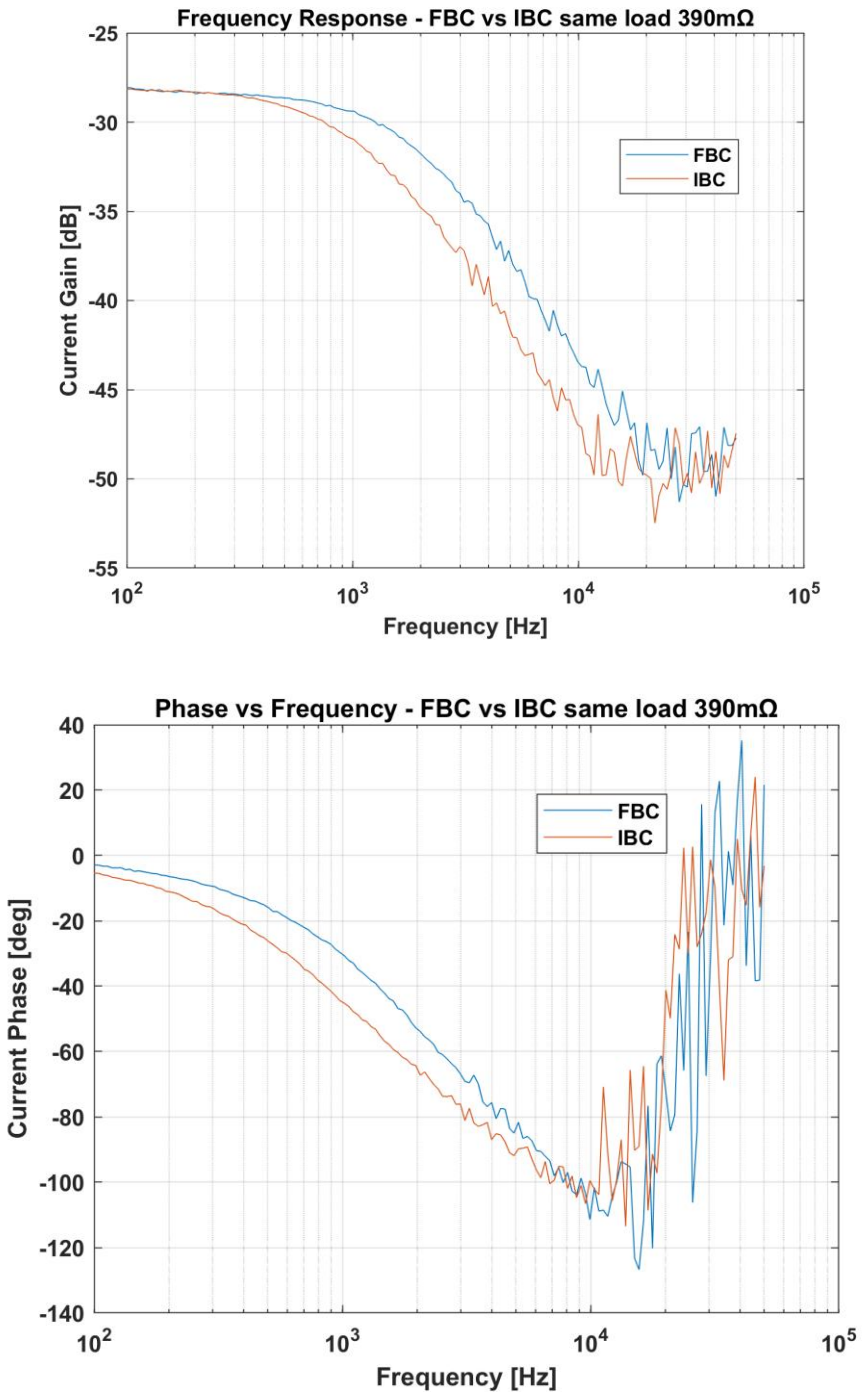

Figure 24: FBC vs IBC cell Current Gain & Phase vs. Frequency – Same Load 390mΩ

Figure 24 depicts that current gain and phase in terms of frequency comparing the FBC 5-inch cell and the IBC cell at the same load. For a higher load of $R_L = 390m\Omega$ we observe a similar pattern for current gain and phase vs frequency.

We still notice differences, namely lower cutoff frequency for the IBC cell with its higher overall capacitance.

Additionally, short-circuit measurements of the frequency response curves with different link distances, i.e. distance between transmitter (light source) and receiver, were obtained.

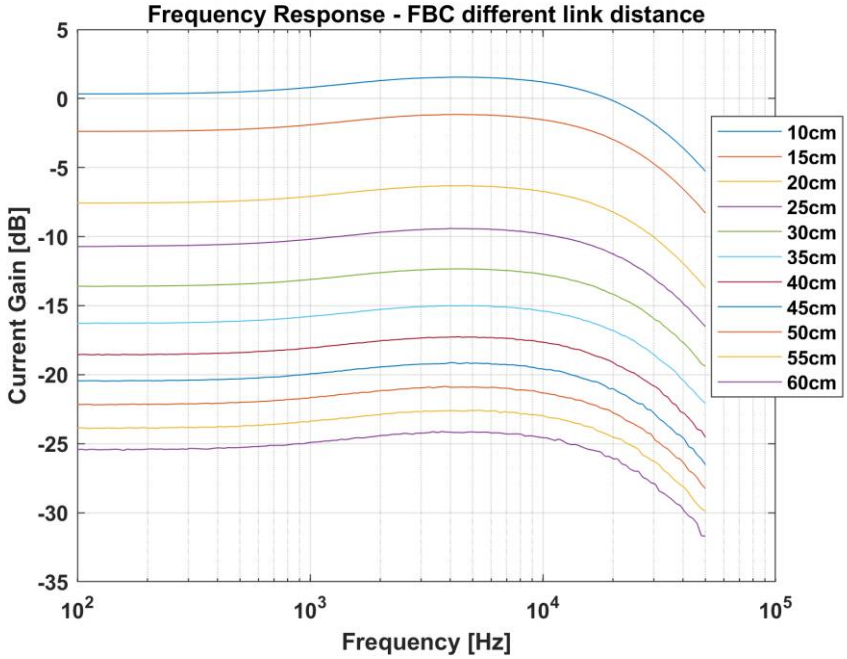

Figure 25: FBC cell Current Gain vs. Frequency for various link distances in short-circuit condition

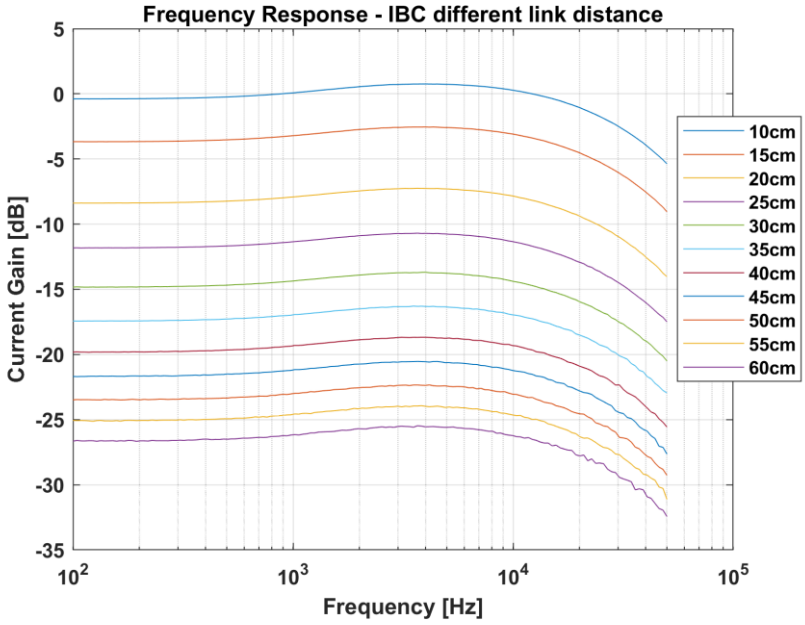

Figure 26: IBC cell Current Gain vs. Frequency for various link distances

Figures 25 and 26 are in agreement with the data we obtained in figures 3-5 of LED light intensity versus link distance. Increasing the link distance obviously has no effect on the communication bandwidth, just alters the current gain and the signal to

noise ratio. A high signal-to-noise ratio is potentially problematic for higher frequencies, especially higher than 10kHz, regardless of the operating point.

4.2 Modelling experimental results

Since we conducted our research with the intention to simultaneously obtain current measurements, starting with short-circuit but ultimately for all operating points, we arrived at the following model by taking the current divider of the circuit in figure 18:

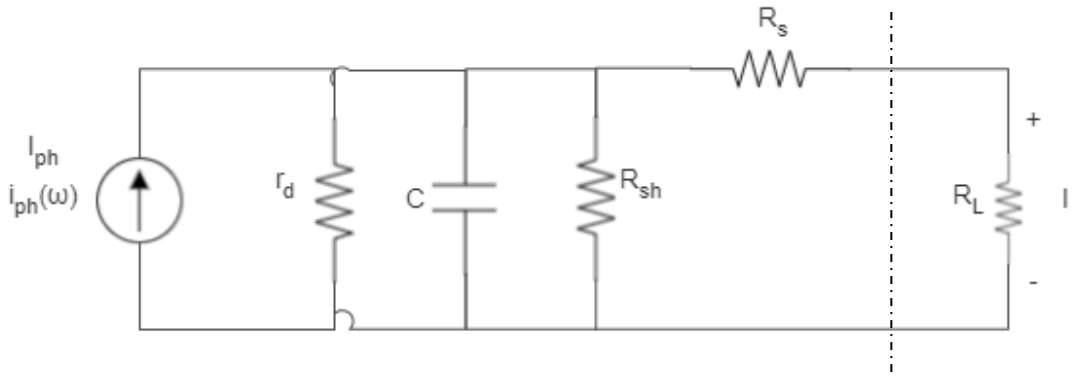

Figure 27: Equivalent circuit model corresponding to experimental setup

The current divider is set up with the impedances of the dynamic resistance, capacitance and shunt resistance grouped together and the impedance of the load and series resistance grouped together. The measured current may expressed as:

$$I_L = I_{PH} \cdot Z(r_d//C//R_{sh})/(R_s + R_L)$$

In chapter 2 we introduced the concept of the gain. According to that definition, the gain therefore ultimately is obtained as:

$$Gain = -20\log\left(\frac{I_L}{i_{PH}(\omega)}\right) - k$$

$$= -20\,log\left|\frac{(\frac{1}{r_d}+j\omega C+\frac{1}{R_{sh}})^{-1}}{(\frac{1}{r_d}+j\omega C+\frac{1}{R_{sh}})^{-1}+(R_S+R_L)}\right| - k \quad (20)$$

Where $\omega = 2\pi f$

The value of the constant k which yields the best fitting results is $k = 20log_{10}(\frac{I_{out}}{I_{in}})$. Essentially, the parameter k translates the frequency response curves toward more negative dB, for the DC value at higher loads.

During our first set of experimental results, we were unable to measure short-circuit current because our current probe had a shunt resistance $R_{sh} = 0.1\Omega$. As a result, we could not achieve a small enough load across the solar cell the have it operate at short-circuit. Ideally, short-circuit current measurements should have a load as close to zero as possible.

Measuring current at short-circuit rather than open-circuit voltage allows us to obtain a greater bandwidth. Figure 8 allows us to observe that a lower the bias voltage, implies lower capacitance, which in turn leads to increased bandwidth. Communication is therefore improved at short-circuit operating conditions.

4.3 Fitting

Using the model in 4.2 and the results in 4.1, we are able to perform a fitting using the MATLAB curve fitting application. Our goal is to derive the values of parameters in our model based on the experimental results. This will also help us give accurate setup recommendations in chapter 5, using the more optimized model (equation 18).

In table 9, we have the comprehensive table of the fitting which shows our model parameters and their values for each cell and for a given load. All the parameters are part of fitting with a coefficient R greater than 0.995 indicating a very good fit of the experimental results and the theoretical model.

Load (mΩ)	Parameters							
	r_d (Ω)		r_{sh} (Ω)		r_s (mΩ)		C (μF)	
	FBC	IBC	FBC	IBC	FBC	IBC	FBC	IBC
390	0.327	0.381	20.15	10.05	7	3.2	50.4	150
470	0.3373	0.1062	15.25	15.67	23	6.1	76.2	275
680	0.3452	0.0580	17.63	11.52	3.6	91	91.7	298

Table 9: Model parameters obtained by fitting the experimental data with the model (Curve Fitting MATLAB)

Notice that, as discussed in chapter 2, bias voltage really affects solar cell capacitance. Namely, higher load implies moving closer to open circuit in terms of operating point.

Let us first delve into the values of dynamic resistance. It does seem very stable when varying the load for the FBC cell. The values for the IBC cell are relatively stable, but with slightly higher variability compared to the FBC cell. The IBC cell has higher capacitance and the fitting application in MATLAB compensates any experimental data points not perfectly within trend by changing the dynamic resistance at the highest load of 680mΩ, since changing the capacitance has too significant of an effect on the frequency response curve.

As far as the shunt resistance is concerned, no significant variability is observed. We expected no significant change in the shunt resistance when changing the operating point. In this parameter, any change comparison between FBC and IBC does not indicate any differences.

The other parameter which theoretically should indicate no significant variability between varying load is the series resistance. The fitting results for this parameter are relatively consistent, but do show an outlier again for the highest load of 0.68Ω by compensating while trying to fit certain experimental data points. A higher load is also likely to yield a greater deviation from the stable range of values the series resistance indicates.

Regarding the capacitance values of the fitting, they seem consistent with theoretical expectations. They are higher for the IBC cell compared to the FBC, confirming once again the fact that the IBC cell is preferable for the sole purpose of harvesting energy. In both cells, the trend that is confirmed is that higher load, i.e. moving from short-circuit to maximum power point and open-circuit implies higher capacitance. As already discussed in Chapter 2, junction capacitance has a greater contribution when operating close to short-circuit and is negligible close to open-circuit. The relative contribution of diffusion capacitance is greater than that of junction capacitance.

5. CONCLUSION

Quantifying the performance of solar cells in terms of energy harvesting and communication may be achieved through examining the tradeoff between the output current/voltage and bandwidth. Two issues are worth noticing in this aspect and became apparent in our research. First, which solar cell is generally more appropriate for which purpose. Second, at which operating point, i.e. a given load, a solar cell yields a "sweet spot" in terms of being decent in harvesting energy without compromising significantly in its communication performance.

In addressing the first question, it is evident from the data in table 7 that the 5-inch FBC monocrystalline Silicon solar cell performs better in terms of communication bandwidth, by having a higher cutoff frequency than the IBC cell. The IBC cutoff frequency is lower, as shown in table 8. For instance, for a load of $R_L = 54m\Omega$ which implies a close to short-circuit operating point for both cells the cutoff frequency of the FBC cell is $f_c = 38.99kHz$ where as that of the IBC cell is $f_c = 27.99kHz$.

Overall, we observe that lower load means faster communication and lower capacitance, according to table 9 of our fitting.

The second question is slightly subjective to address, since the operating point where one is happy with both energy harvesting and communication depends on where one places more value. In practice, a potential application would imply that energy-sufficiency is achieved, namely that we achieve communication without requiring an external power source. For our purposes, we place more value in communication bandwidth, so we phrase the problem in terms of what is the lowest output current of our solar cell where energy harvesting satisfies our needs, while maintaining high bandwidth.

The mathematical model that describes the current measurements obtained experimentally is equation 20:

$$\frac{I_L}{i_{PH}(\omega)} = 20\,log\left|\frac{(\frac{1}{r}+\frac{1}{j\omega C}+\frac{1}{R_{sh}})^{-1}}{(\frac{1}{r}+\frac{1}{j\omega C}+\frac{1}{R_{sh}})^{-1}+(R_s+R_L)}\right| - k$$

Where $\omega = 2\pi f$ and $k = 20log_{10}(\frac{I_{out}}{I_{in}})$.

This model yields consistent values for the equivalent circuit parameters.

The other model which became significant throughout our research is the AC+DC energy harvesting and communication model with two branches.

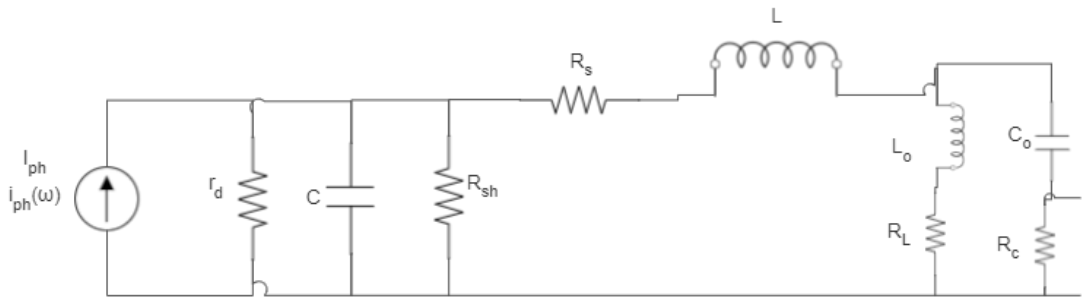

Figure 30: Equivalent circuit for AC+DC simultaneous energy harvesting and communication [6]

In order to provide concrete setup recommendations, we may narrow down the parameters of the energy harvesting and communication model with the branches containing R_c,C_o,L_o and R_l. Our methodology for achieving this is by designing a combination of a low-pass RL filter and a high-pass RC filter which splits DC and AC signal and allows for both energy harvesting and communication, as shown in chapter 2.4.

The mathematical aspect of the filter design are analyzed in detail in Chapter 2.4 and the comprehensive tables of parameters for both cells are the following:

Rl (Ω)	fc (kHz)	Rc (Ω)	Co (µF)	Lo (µH)
0.013	37,41	0.5	0.12	0.06
0.054	37.41	0.5	0.46	0.23
0.085	37.41	0.5	0.72	0.36
0.1	37.41	0.5	0.86	0.43
0.270	12.23	0.5	7	3.5
0.310	1540	0.5	64	32
0.39	1744	0.5	72	36
0.47	1895	0.5	78	39
0.68	1975	0.5	110	55

Table 10: Compenent values of two-branch model for FBC cell

Rl (Ω)	fc (kHz)	Rc (Ω)	Co (µF)	Lo (µH)
0.013	27.99	0.5	0.14	0.07
0.054	27.99	0.5	0.62	0.31
0.085	27.99	0.5	0.96	0.48
0.1	25.77	0.5	1.24	0.62
0.17	5.12	0.5	10.6	5.3
0.270	4.16	0.5	20.6	10.3
0.39	1.06	0.5	117.2	58.6
0.47	1.10	0.5	136	68
0.68	1.06	0.5	204	102

Table 11: Compenent values of two-branch model for IBC cell

Consequently, if we were to design an experiment with single-value components which would allow us to facilitate both energy harvesting and communication for any value of the load which we were able to measure, the branch values of a recommended setup are shown in table 12:

	FBC	IBC
Rc	0.5Ω	0.5Ω
Co	50µF	10µF
Lo	25µF	5 µF

Table 12: Compenent values of two-branch model for both cells

We assume that the inductor of the energy harvesting branch does not influence the operating point of the cell. This is certainly true for low frequencies and is an acceptable assumption for the range of frequencies of the obtained measurements. Hence, the operating point in the 2-branch model is solely affected by the value of the resistive load R_L.

BIBLIOGRAPHY

1. Haas, H.; Yin, L.;Wang, Y.; Chen, C. What is LiFi? J. Lightwave Technol. 2016, 34, 1533–1543.
2. P. J. Reddy, Science & Technology of Photovoltaics, 2nd ed. Leiden, The Netherlands: CRC Press, 2010.
3. N. Lorrière et al., "Photovoltaic Solar Cells for Outdoor LiFi Communications," in Journal of Lightwave Technology, vol. 38, no. 15, pp. 3822-3831, 1 Aug.1, 2020.
4. N. A. Mica et al., “Triple-cation perovskite solar cells for visible light communications,” Photon. Res., vol. 8, no. 8, pp. A16–A24, Aug. 2020. 1 L. Varshney, “Transporting information and energy simultaneously,” in IEEE International Symposium on Information Theory (ISIT), 2008, pp. 1612–1616.
5. Wang, Z.; Tsonev, D.; Videv, S.; Haas, H. Towards Self-powered solar panel receiver for optical wireless communication. In Proceedings of the 2014 IEEE International Conference on Communications (ICC), Sydney, NSW, Australia, 10–14 June 2014.
6. Wang, Z.; Tsonev, D.; Videv, S.; Haas, H. On the design of a solar panel receiver for optical wireless communication with simultaneous energy harvesting. IEEE J. Sel. Areas Commun. 2015, 33, 1612–1623.
7. Fakidis, J.; Videv, S.; Helmers, H.; Haas, H. 0.5-Gb/s OFDM-Based Laser Data and Power Transfer Using a GaAs Photovoltaic cell. IEEE Photonics Technol. Lett. 2018, 30, 841–844.
8. Das S, Poves E, Fakidis J, Sparks A, Videv S, Haas H. Towards Energy Neutral Wireless Communications: Photovoltaic Cells to Connect Remote Areas. Energies. 2019; 12(19):3772.
9. S.-M. Kim and J.-S. Won, “Simultaneous reception of visible light communication and optical energy using a solar cell receiver,” in Proc. IEEE Int. Conf. ICT Convergence, 2013, pp. 896–897
10. S. Zhang et al., “Organic solar cells as high-speed data detectors for visible light communication,” Optica, vol. 2, no. 7, pp. 607–610, Jul. 2015.
11. H. Haas, E. Sarbazi, H. Marshoud, and J. Fakidis, “Visible-light communications and light fidelity,” in Optical Fiber Telecommunications VII, 1st ed. London, U.K.: Academic, 2019, pp. 443–493.
12. Fakidis and Lin, Simultaneous Wireless Data and Power Transfer for a 1-Gb/s GaAs VCSEL and Photovoltaic IEEE Photonics Technology Letters 32(19):1277 IEEE 2020 1041-1135.
13. Overview of Photovoltaic Module Performance Modeling Approaches Joshua S. Stein PhD. Sandia National Laboratories, Albuquerque, NM USA 7 th PVPMC Workshop on Energy Rating and Module Performance Modeling Lugano, Switzerland March 30-31, 2017.
14. Tian, H., Mancilla-David, F., Ellis, K., Muljadi, E., & Jenkins, P.E. (2012). Detailed Performance Model for Photovoltaic Systems: Preprint
15. Neamen, D. A. Semiconductor physics and devices: Basic principles (4th ed.). McGraw-Hill (2012).
16. Zaraket, Jean & Sidawi, Jihad & Aillerie, M. & Salame, Chafic. (2015). Capacitance Evolution of Photovoltaic Solar Modules Under the Influence of Electrical Stress. Energy Procedia. 74. 1466-1475. 10.1016/j.egypro.2015.07.795.
17. Salach-Bielecki, R & Pisarkiewicz, Tadeusz & Stapinski, T. & Wójcik, P. (2004). Influence of junction parameters on the open circuit voltage decay in solar cells. Opto-electronics Review. 12.
18. Cotfas et al. Solar Cell Capacitance Determination Based on an RLC Resonant Circuit. Energies. 2018; 11(3):672. https://doi.org/10.3390/en11030672
19. Kumar, R.A.; Suresh, M.S.; Nagaraju, J. Silicon (BSFR) solar cell AC parameters at different temperatures. Sol. Energy Mater. Sol. Cells **2005**, 85, 397–406.
20. Anantha Krishna, H.; Misra, N.K.; Suresh, M.S. Use of solar cells for measuring temperature of solar cell blanket in spacecrafts. Sol. Energy Mater. Sol. Cells 2012, 102, 184–188

21. Kumar, S.; Singh, P.K.; Chilana, G.S. Study of silicon solar cell at different intensities of illumination and wavelengths using impedance spectroscopy. Sol. Energy Mater. Sol. Cells 2009, 93, 1881–1884.
22. Hameiri, Z. Photovoltaics literature survey (No. 125). Progress Photovoltaics Res. Appl. 2016, 24, 405–407.
23. Saltsman, S.O. The Silicon Solar Cell as an Optical Detector; Florida Technological University: Orlando, FL, USA, 1976.
24. Rana, F. Photodetectors and Solar Cells. In Semiconductor Optoelectronics; Rana, F., Ed.; Cornell University: Ithaca, NY, USA.
25. Texas Instruments Inc. BQ24650 High Efficiency Synchronous Switch-Mode Charger Controller—Solar battery charger.
26. L. Varshney, "Transporting information and energy simultaneously," in IEEE International Symposium on Information Theory (ISIT), 2008, pp. 1612–1616.
27. Tavakkolnia, I., Jagadamma, L.K., Bian, R. et al. Organic photovoltaics for simultaneous energy harvesting and high-speed MIMO optical wireless communications. Light Sci Appl 10, 41 (2021).
28. Texas Instruments Inc. BQ24650 High Efficiency Synchronous Switch-Mode Charger Controller—Solar battery charger.
29. H. Rauschenbach, Solar Cell Array Design Handbook. Berlin, Germany:Springer, 1980.
30. Smets, A., Jager, K., Olindo, I., Swaaij, R. ., & Zeman, M. (2016). Solar energy: The physics and engineering of photovoltaic conversion, technologies and systems. Cambridge: UIT Cambridge
31. SunPower Gen 3 Cell – Mono c-Si 166mm datasheet [revised January 2019]
32. IBC-Solar AKW datasheet Mono c-Si IBC solar cell
33. Chowdhury, Mostafa & Hossan, Md Tanvir & Islam, Amirul & Jang, Yeong Min. (2018). A Comparative Survey of Optical Wireless Technologies: Architectures and Applications. IEEE Access. PP. 1-1. 10.1109/ACCESS.2018.2792419.
34. Digilent Analog Discovery 2 USB Oscilloscope. https://digilent.com/shop/analog-discovery-2-100ms-s-usb-oscilloscope-logic-analyzer-and-variable-power-supply/
35. Michael, IEEE Conversion Guide: Solar Irradiance and Lux Illuminance., https://ieee-dataport.org/open-access/conversion-guide-solar-irradiance-and-lux-illuminance (2019)

Appendix A – Useful Equations

$$I_{ph} = \frac{I_o}{e^{-\frac{V_{in}}{V_t}}}$$

Voltage Gain $G[dB] = -20\log\left(\frac{V_{out}}{V_{in}}\right)$

Current Gain $G[dB] = -20\log\left(\frac{I_{out}}{I_{in}}\right)$

Capacitance $C = C_d + C_T$

Shockley diode equation: $V_{oc} = V_t \cdot \ln\left(\frac{I_{ph}}{I_o} + 1\right)$

Impedance in Frequency domain: $Z(f) = \frac{V_{oc}^F(f)}{I_{ph}^F(f)} = \frac{r_d}{1+j\cdot 2\pi r_d \cdot C_d \cdot f}$

$$Z(f) = \frac{V_{oc}^F(f)}{I_{ph}^F(f)} = \frac{r_d}{1 + j \cdot 2\pi \cdot \tau \cdot f}$$

$$\frac{Gain}{1 + j\frac{f}{f_c}}$$

3-dB cutoff frequency: $f_c = \frac{1}{2\pi\tau}$

Solar Panel model for communication

Frequency response: $\left|\frac{\boldsymbol{v(\omega)^2}}{\boldsymbol{i_{PH}(\omega)}}\right|^2 = \left|\frac{\frac{\boldsymbol{R_C}}{\boldsymbol{R_X}}}{\frac{\boldsymbol{1}}{\boldsymbol{r}}+\frac{\boldsymbol{1}}{\boldsymbol{j\omega C}}+\frac{\boldsymbol{1}}{\boldsymbol{R_{sh}}}+\frac{\boldsymbol{1}}{\boldsymbol{R_X}}}\right|^2$

$$R_X = R_S + j\omega L + \frac{1}{j\omega C_0} + R_C$$

Solar Panel model for communication and energy harvesting

Frequency response: $\left|\frac{\boldsymbol{v(\omega)^2}}{\boldsymbol{i_{PH}(\omega)}}\right|^2 = \left|\frac{\frac{\boldsymbol{R_{LC}}}{\boldsymbol{R_S+j\omega L+R_{LC}}}\cdot\frac{\boldsymbol{R_C}}{\frac{\boldsymbol{1}}{\boldsymbol{j\omega C_o+R_C}}}}{\frac{\boldsymbol{1}}{\boldsymbol{r}}+\frac{\boldsymbol{1}}{\boldsymbol{j\omega C}}+\frac{\boldsymbol{1}}{\boldsymbol{R_{sh}}}+\frac{\boldsymbol{1}}{\boldsymbol{R_S+j\omega L+R_{LC}}}}\right|^2$

Resistance of the parallel network:

$$R_{LC} = \frac{1}{\frac{1}{j\omega L_o + R_L} + \frac{1}{\frac{1}{j\omega C_o} + R_C}}$$

$$R_{LC} = \frac{j\omega L_o - \omega^2 L_o C_o R_C + R_L + R_L R_C j\omega C_o}{1 + j\omega C_o R_C - \omega^2 C_o L_o + j\omega C_o R_L}$$

$$v(\omega)\cdot\frac{1}{r} + \frac{1}{j\omega C} + \frac{1}{R_{sh}} + \frac{1}{R_X} = \frac{R_{LC}}{R_S + j\omega L + R_{LC}} \cdot \frac{R_C \cdot j\omega C_o}{1 + j\omega C_o R_C} \cdot i_{ph}(\omega)$$

$$R_X = R_S + j\omega L + \frac{1}{j\omega C_0} + R_C$$

$$\lim_{\omega \to 0} R_{LC} = R_L$$

$$\tau_{RC} = (R_S + R_L) \cdot C$$

$$R_L = \infty$$

$$\lim_{\omega \to \infty} R_{LC} = \lim_{\omega \to \infty} \frac{R_L}{1 + j\omega C_0 R_S + j\omega C_0 R_L} =$$

$$\lim_{\omega \to 0} \frac{v(\omega)}{i_{PH}(\omega)} = \frac{R_{LC}(R_S + R_{LC})^{-1}}{r^{-1} + R_{SH}^{-1} + (R_S + R_{LC})^{-1}}$$

$$\frac{i_{PH}(\omega)}{v(\omega)} = \frac{R_{LC} \cdot R_C(R_S + j\omega L + R_{LC})^{-1}((j\omega C_0)^{-1} + R_C^{-1})}{r^{-1} + j\omega C + R_{SH}^{-1} + (R_S + j\omega L + R_{LC})^{-1}}$$

Lambertian rule for modeling the light source:

$$P_r = P_t \cdot \frac{m+1}{2\pi d^2} \cos(\varphi)^m \cdot G_{filter} \cdot G_{concentrator} \cdot \cos(\psi)$$

Appendix B

Determining capacitance from experimental data using a square signal

There are also different approaches to determine the capacitance of the cell if we are sending a square signal (for instance, a square signal from an LED matrix source).

For MPP using a square signal:

$$C_{MPP} = \frac{\tau}{R}$$

In order to determine the time constant we need to find how long it takes to reach 63.2% of the final value of the voltage. This value is derived by a factor of $e^{-1} = 0.3678$. The response of the system is $v(t) = V_o(1 - e^{-1})$.

We need to compute these both for the LED voltage in AC as well as for the PV voltage in AC. Then, we take the difference of the time constants to find the capacitance at the maximum power point.

Let us start with the LED computation. In figure 32, we compute the different between the initial and final value and determine where the 63.2% value lies.

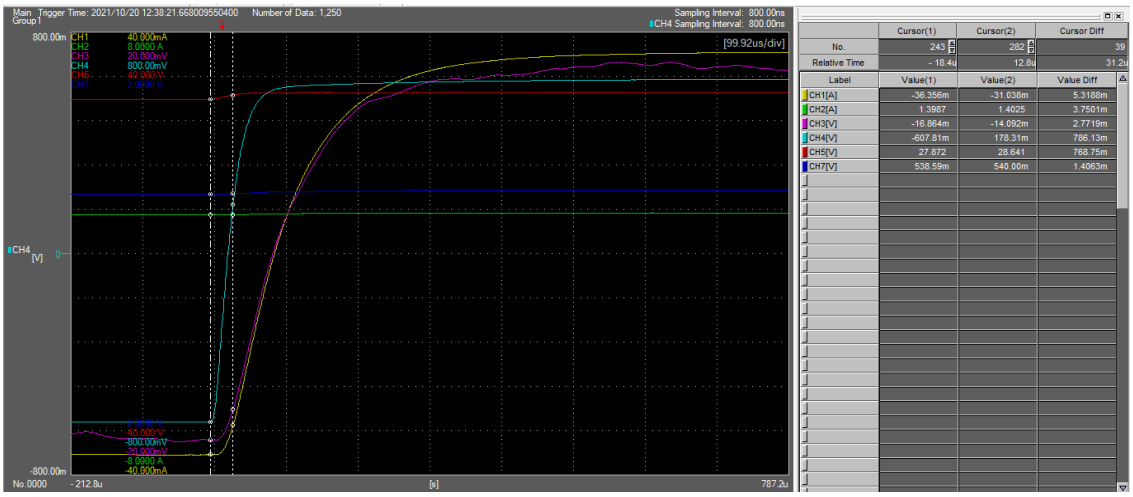

Figure 32: Determining the time constant at MPP for the LED

The range of the initial to final value is $628mV + 610mV = 1.238V$.

Therefore, we are looking for the time it takes to reach $63.2\% \cdot 1.238V = 786mV$

Which occurs at $172mV$ which is $\tau_{LED} = 31.2\mu s$

Similarly, for the FBC 5-inch cell we obtain:

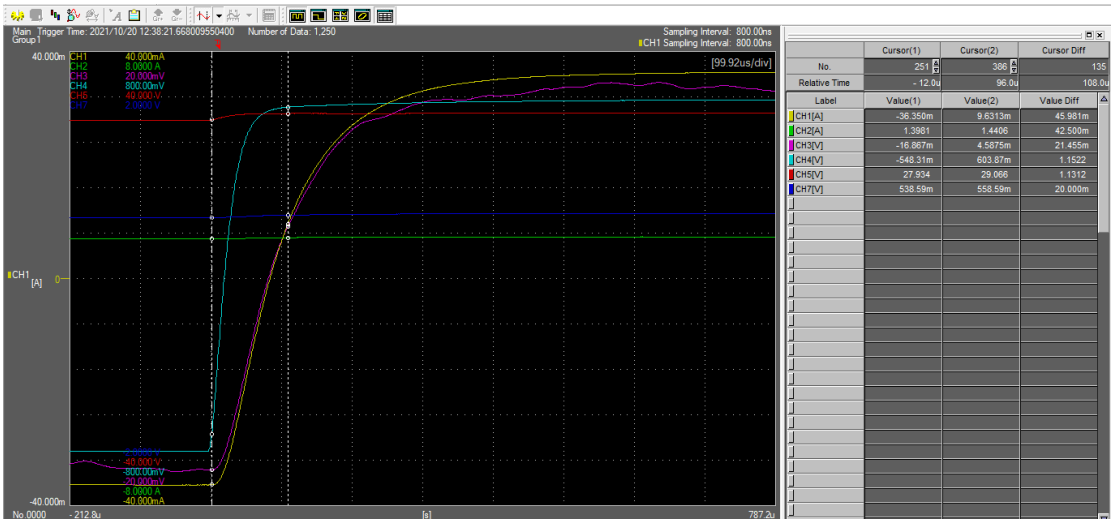

Figure 33: Determining the time constant at MPP for the FBC 5-inch cell

The range of the initial to final value is $-(-16.87mV) + 17.25mV = 34.12mV$

Thus, we are looking for the time it takes to reach $63.2\% \cdot 34.12mV = 786mV$, which occurs at $4.69mV$, which is $\tau_{LED} = 98\mu s$

Finally, the capacitance

$$C_{MPP} = \frac{\tau}{R} = \frac{98 \cdot 10^{-6} - 38 \cdot 10^{-6}}{\frac{V_{MPP}}{I_{MPP}}} = \frac{31 \cdot 10^{-6}}{\frac{570\text{mV}}{1.4625\text{A}}} = 77\mu F$$

For Short-Circuit (SC), using a square signal

we follow the same process using the data in figure 34 below:

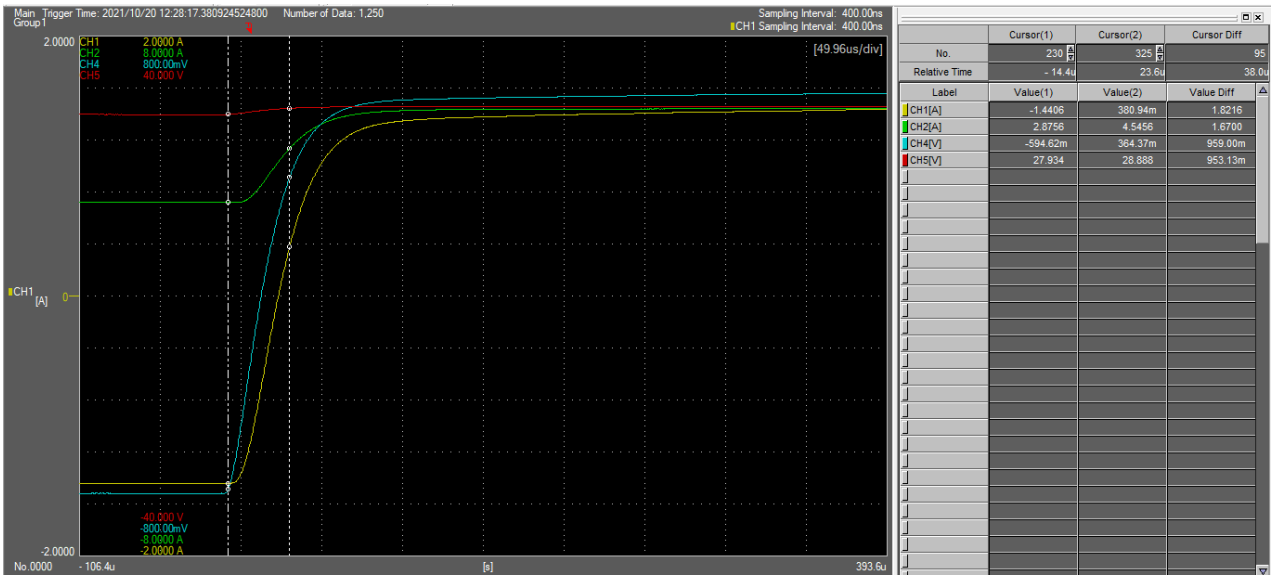

Figure 34: Determining the time constant at SC for the FBC 5-inch cell (Channel 1: PV current in AC)

The range of current values of PV short-circuit current in AC is $-(-1.44A) + 1.42A = 2.86A$

The value of interest is $63.2\% \cdot 2.86A = 1.82A$

The time constant is the time it takes to reach 0.37A which is $\tau_{PV} = 38\mu s$

Hence, the capacitance of the cell at SC is

$$C_{SC} = \frac{\tau}{R_{total}} = \frac{12 \cdot 10^{-6}}{R_s + (\frac{1}{r_d} + \frac{1}{R_{sh}})^{-1}} = \frac{12 \cdot 10^{-6}}{0.00266 + (\frac{1}{2.76 \cdot 10^6} + \frac{1}{2.54})^{-1}} = 16\mu F$$

Appendix C

MATLAB code

MATLAB Curve Fitting model code:

*20*log10(abs(((r*rsh)/(r+rsh))./(((r*rsh)/(r+rsh))+rs+rl+1i*pi*x.*(rs+rl)*((r*rsh)/(r+rsh))*c)))-*

*20*log10(3.98)*

Generalized (2-Branch) VLC MATLAB Model:

```
clc
% Author: Ioannis Skourtis
% TU Delft - PVMD Group
% I.Skourtis@student.tudelft.nl
% I.Skourtis@student.tudelft.nl
%%
k = 1.3806503e-23;   %Boltzmann [J/K]
q = 1.60217646e-19;  %Electron charge [C]

Rs=0.0036; %series resistance [Ω]
Rp=17.63; %shunt resistance [Ω]

Ki=0.043; %current temperature constant
Kv=-0.00317; %voltage temperature constant

T=298;
Tn=298; %STC Temperature  [K]
Gn=1000; %STC Irradiance  [W/m^2]
G=1000;

%Iph=8.22; %photocurrent [A]

Voc=0.654; %open-circuit voltage [V]
Isc=9.61; %short-circuit current [A]

Ns=1; %number of cells in series

A = 1; %diode ideality factor


%%
dT=T-Tn;
Vt=(k*A*T*Ns)/q;

Iph =(Isc+Ki*dT)*(G/Gn); %photo current

I0 =(Isc+Ki*dT)/exp(((Voc+Kv*dT)/Vt)-1);  %Saturation current

%Ip = ((V)+(I * Rs)) / Rp; %shunt current

%Id=exp(((V*Ns+Rs*I)/Vt)-1)*Io; ONLY FOR ENERGY HARVESTING - DC
```

```
%I=Iph+Id-Ip; ONLY FOR ENERGY HARVESTING - DC

%% We replaced the forward-biased diode with a dynamic resistance and
capacitance for AC small signal model
% r = (Vt/Io)*e^(V/Vt);

% C = τ/r

% Specifically for Open-Circuit conditions

% r = Vt/Iph;

r = 2.5;  % [Ω]

C = 298e-6; %short-circuit value [F]

%C2 = 10e-6; %open-circuit value [F]


%% We add an inductor L in series with Rs to model wire connections
to the solar panel

L = 120e-9; %[H]

% We add an energy harvesting branch with inductor Lo and load
resistance Rl
Lo = 100e-6; % Inductance [H]
Rl = 0.1; % Load Resistance [Ω]

% We add a communication branch with capacitor Co and resistor Rc -
values

Co = 100e-6; % [F]

Rc = 0.5;  % [Ω]

% The resistance of the two branches in parallel is
%Rlc = 1/([(j*ω*Lo + Rl)^(-1) + (1/[(jωCo)^(-1) + Rc ^(-1)]));
%Rlc = (1/(((1j*(2*pi*x)*Lo + Rl)^(-1) + (1/((1j*(2*pi*x)*Co)^(-1) +
Rc ^(-1))))));
%The frequency response is
% |v(ω)/iph(ω)|^(2)= |(Rlc* Rc)/[(Rs + j    ωL +
Rlc)*((1/jωCo)+Rc)]/(r^(-1)+(jωC)+Rp^(-1)+(Rs + jωL + Rlc)^(-
1))|^(2);


fmax = 40000;
x = 100:1:fmax;

y1 = (((1./(1./(1j*(2*pi*x)*Lo + Rl)) + (1./(1./(1j*(2*pi*x)*Co)
+(1./Rc)))).* Rc) ./ ((Rs + 1j*(2*pi*x)*L + (1./(1./(1j*(2*pi*x)*Lo +
Rl)) + (1./(1./(1j*(2*pi*x)*Co) +(1./Rc))))).*(1./((1j*(2*pi*x)*Co)+
Rc)))./((1./r)+(1./(1j*(2*pi*x)*C))+(1./Rp)+(1./(Rs +
(1j*(2*pi*x)*L) + (1./(1./(1j*(2*pi*x)*Lo + Rl)) +
(1./(1./(1j*(2*pi*x)*Co) +(1./Rc)))))));
```

```
figure;
title('Frequency Response - FBC OC')
xlabel('Frequency [Hz]');ylabel('Current Gain [dB]')
semilogx(x,real(y1));
grid on
```